Raman quantification factor calibration for CO-CO2 gas mixture in synthetic fluid inclusions: Application to oxygen fugacity calculation in magmatic systems

Yann Morizet, Michaël Paris, Fabrice Gaillard, Bruno Scaillet

Raman quantification factor calibration for CO-CO_2 gas mixture in synthetic fluid inclusions: Application to oxygen fugacity calculation in magmatic systems.

Y. Morizet[a], M. Paris[b], F. Gaillard[c], B. Scaillet[c]

[a] Laboratoire de Planétologie et Géodynamique de Nantes (LPGN), Université de Nantes

CNRS/INSU – UMR CNRS 6112.

2 rue de la Houssinière, BP 92208.

44322 Nantes Cedex 3 (FRANCE).

[b] Institut des Matériaux Jean Rouxel (IMN), Université de Nantes

CNRS/INSU – UMR CNRS 6502

2 rue de la Houssinière, BP 32229.

44322 Nantes Cedex 3 (FRANCE).

[c] Institut des Sciences de la Terre d'Orléans (ISTO), Université d'Orléans

CNRS/INSU – UMR CNRS 6113

1A rue de la Ferollerie.

45071 Orleans Cedex 2 (FRANCE)

Corresponding author: Dr Yann Morizet

Permanent address:

Laboratoire de Planétologie et Géodynamique de Nantes (LPGN), Université de Nantes

CNRS/INSU – UMR CNRS 6112

2 rue de la Houssinière, BP 92208.

44322 Nantes Cedex 3 (FRANCE).

Email: yann.morizet@univ-nantes.fr

Tel: +33 (0) 2 5112 5491

Fax: +33 (0) 2 5112 5268

Abstract:

With a combined approach using Solid State ^{13}C-MAS NMR and Laser Raman Microspectroscopy, we investigated the CO_2-CO gas composition ($X(CO_2)$) in fluid inclusions synthesised under high pressure (200-300 MPa), high temperature (1225-1250°C) and reducing conditions ($17 < P(H_2) < 62$ bars). Fluid inclusions are entrapped in a volatile-bearing basaltic glass which was characterized by FTIR for determining the water solubility (H_2O^m).

^{13}C-MAS NMR is used as a standard analysis for determining the $X(CO_2)$. The Raman quantification factors between $^{13}CO_2$ and ^{13}CO is determined from peak area (F-factor), peak height (G-factor) and according to the Placzek's polarizability theory. The calibration is derived for both CO_2 Fermi diad resonances: $2\nu_2$ and ν_1.

We obtain similar values for the main CO_2 resonance ($2\nu_2$) with 1.956 and 1.809 for F and G respectively. Results are consistent with the fact that peak height and area will measure the same quantity. For ν_1, multiple calibration trends are observed. The different trends are explained by the different $^{13}C/^{12}C$ ratio observed in between the samples. However, we suggest that such resonance is not suitable for determining the fluid inclusion compositions.

We extended the ^{13}C results for calibrating the F- and G-factors for $^{12}CO_2$-^{12}CO gas mixture in the fluid inclusions and for the main CO_2 resonance. For $^{12}CO_2$-^{12}CO mixture, F and G values are 1.856 and 1.756 which is in the same order as the derived values for ^{13}C species. Thus, we propose that no significant $^{13}C/^{12}C$ fractionation occurs in the fluid phase and both isotopes will behave in a similar way.

Using the derived calibration for ^{12}C and ^{13}C species, the $X(CO_2)$ in the fluid phase was recalculated. Results are similar for both isotopes witnessing the similar behaviour of ^{12}C and ^{13}C fluid species during the experiments.

The log $f(O_2)$ experienced by each sample has been calculated through a thermodynamic approach using 2 independent methods. The log $f(O_2)$ calculated from the H_2O^m in the glass and the $X(CO_2)$ in the fluid phase are in good agreement. Large discrepancy is observed for low H_2O^m content which gives lower log $f(O_2)$ value than expected from experimental conditions. Large uncertainties on the H_2O^m measurements will induce a very approximate value for the log $f(O_2)$. This method may not be accurate enough at low H_2O^m and using the $X(CO_2)$ in the fluid phase would therefore provide a better estimate of the log $f(O_2)$.

Keywords: Fluid inclusion, Raman spectroscopy, Solid State NMR, Carbon dioxide, oxygen fugacity.

1 Introduction:

Volatiles are ubiquitous components implied in many geological systems. In particular, CO_2 and H_2O are the two most abundant volatiles emitted at volcanic centres (Gerlach and Graeber, 1985; Symonds et al., 1994; Jambon, 1994; Morizet et al., 2002). CO_2 is usually present in magmas with moderately oxidised conditions. However, under more reducing conditions other volatiles become stable such as CO, CH_4 (Kadik et al., 2004). Although the distinction should be made between volatiles dissolved in the melt and volatiles implied in the fluid phase in equilibrium with the melt, both need to be considered as parts of a given system. The solubilities of H_2O and CO_2 are controlled by H_2O and CO_2 fluid fugacities (Dixon et al. 1995; Dixon, 1997) for a given melt composition at fixed P and T.

In magmatic systems, upon decompression volatiles exsolve the melt phase to be stored in the fluid phase. This observation is even more verified for CO_2 which has a low solubility compared to H_2O (e.g., Blank and Brooker, 1994; Dixon, 1997; Morizet et al., 2002). The fluid phase is partly preserved as inclusions within minerals or within the silicate melt phase itself. Fluid inclusions study can provide valuable information on the Earth interiors volatiles content and degassing (Frezzotti and Peccerillo, 2007).

Estimating or calculating the oxygen fugacity ($f(O_2)$) in Earth materials is a recurring problem. The $f(O_2)$ cannot be measured directly except in volcanic gases (Symonds et al., 1994). In the melt phase, the $f(O_2)$ may be estimated using several methods. Within the melt, the Fe^{3+}/Fe^{2+} is a proxy for the $f(O_2)$ as described by Kress and Carmichael (1991) or Bezos and Humler (2005). The H_2O content in the melt depends on the $f(H_2O)$ in the fluid which is in turn a function of the $f(O_2)$ according to the reaction:

$$H_2^{fl} + \frac{1}{2} O_2^{fl} \leftrightarrow H_2O^{fl} \qquad (1)$$

The $f(H_2O)$ is first estimated from existing models (e.g. Dixon et al., 1995). Then, with a known $f(H_2)$, one can estimate the $f(O_2)$.

The $f(O_2)$ can also be calculated from the equilibrium of carbon-bearing volatile species and according to several reaction such as:

$$CO_2^{fl} \leftrightarrow CO^{fl} + \frac{1}{2} O_2^{fl} \qquad (2)$$

$$CO_2^{fl} + 2H_2^{fl} \leftrightarrow CH_4{}^{fl} + O_2^{fl} \qquad (3)$$

Either reaction can be used to calculate $f(O_2)$ depending on the species abundances. The first reaction is commonly used in moderately reducing conditions, such as with present day MORB (Pawley et al. 1992). CO_2-rich fluid inclusions are also very common in shallow mantle rocks (Andersen and Neumann, 2001).

The second reaction occurs with more severe reducing conditions (Holloway, 1987; Kadik et al., 2004) where CH_4 is the dominant species and is supposed to have been a major control of the degassing during the Archean period (Arculus, 1985). CH_4 is identified in the fluid phase entrapped in inclusions for particular geological settings. Beeskow et al. (2005) analysed CH_4-CO_2 fluid inclusions in quartz collected from a coalfield in South Wales. Liu and Fei (2006) identified CH_4 in olivine-hosted fluid inclusions from Paleozoic ophiolites.

The investigation on the composition of the fluid phase is of great interest for the understanding of the Earth degassing. It thus appears compulsory to study the composition of the fluid phase as it provides valuable information on the redox state of the Earth mantle.

1.1 Fluid inclusions analyses: Quantification of the fluid species.

Qualitative and quantitative analyses of fluid inclusions can be achieved with several techniques either destructive or non-destructive. The different approaches are reviewed elsewhere (Dubessy et al., 1989; Roedder, 1990; Boiron and Dubessy, 1994; Shepherd et al., 1998).

Laser Raman Microspectrometry (LRM) has been widely used for fluid inclusion analyses as it is non-destructive and not time consuming (Roedder, 1990; Burke 2001). On the other hand, Raman is virtually non-quantitative (McMillan, 1984) and can only be used with relevant calibration with standards with known composition (Wopenka and Pasteris, 1987; Dubessy et al., 1989; Seitz et al.; 1993). LRM Non-quantitative aspects arise from the lack of knowledge on the analysed sample and therefore the number of excited molecule. Thus only the mole ratios between species are usually used.

In fluid inclusion composition analyses, LRM technique is coupled with other techniques such as microthermometry (e.g. Bergman and Dubessy, 1984; Chen et al., 2004), FTIR (Wopenka et al., 1990), LA-ICP-MS (e.g. Shepherd et al., 1998; Stalder et al., 1998; Günther et al., 1998) or even NMR (Dereppe et al., 1994).

NMR is the only bulk non-destructive method. It can be used to investigate various elements: ^{23}Na, ^{29}Si, ^{27}Al or/and ^{13}C in solid state (Kohn et al. 1991; Neuville et al., 2006; Lee and Stebbins, 2003) but also ^{35}Cl in fluid inclusions (Sherriff et al., 1987). Although it appears to be a powerful technique, it has sample requirements: 1) Fe-free composition, 2) relatively large sample (> 100 mg) and 3) possible isotopic enrichment of elements with nuclear spin.

To be quantitative LRM requires knowledge of the spectroscopic behaviour of the molecular species as a function of the molecular environment. Combining LRM with MAS NMR is one adequate solution for achieving qualitative and quantitative analyses of fluid inclusions.

The gas species molar fraction (X) in fluid inclusion can be determined according to the following equation:

$$X_a = \frac{\frac{A_a}{\sigma_a \zeta_a}}{\sum_i \frac{A_i}{\sigma_i \zeta_i}} = \frac{\frac{A_a}{F_a}}{\sum_i \frac{A_i}{F_i}} = \frac{\frac{H_a}{G_a}}{\sum_i \frac{H_i}{G_i}} \qquad (4)$$

where X_a is the molar fraction of the species *a*, A stands for the area of the species observed by LRM, σ is the Raman cross-section coefficient of a given vibrational Raman active mode of a specified molecule and ζ the Raman spectrometer instrumental efficiency for the Raman active mode of the specified molecule and at a given excitation wavelength. ζ is specific to one spectrometer and may be totally different for another spectrometer. Wopenka and Pasteris (1987) combined these two parameters and defined F as the integrated Raman quantification factor. Similarly, a linear Raman quantification factor G can be defined and related to the absolute height of the peak (H).

σ is wavelength dependent (Dubessy et al., 1989; Burke, 2001). ζ is a parameter specific to each Raman apparatus and therefore needs to be determined for each Raman spectrometer (Kerkhof and Kisch, 1993). As a result, if one needs to perform LRM quantitative analyses of fluid inclusions, it is imperative to calibrate those parameters. Many studies (e.g. Wopenka and Pasteris, 1987; Kherkhof, 1988a; Chou et al., 1990)

suggested acquiring such empirical calibration through the use of standards with known compositions.

In our study we combined two methods (NMR and LRM) to calibrate the Raman quantification factor, F, for $^{12\text{-}13}CO_2$ and $^{12\text{-}13}CO$. One major advantage is the fully quantitative aspect of the NMR (the intensity of the signal is directly proportional to the molar fraction of the identified species). As a bulk method, NMR will averaged out the compositional heterogeneity which can observed by LRM from one fluid inclusion to another.

The review by Burke (2001) lists the reported values for various gas species σ. Currently, there is a lack of knowledge concerning the calibration of ^{13}C species. For the $2\nu_2$ $^{13}CO_2$ vibration (overtone of the bending vibration ν_2 for a CO_2 molecule), a value of 1.5 for σ at 514 nm has been used by several authors (Rosasco et al., 1975; Dhamelincourt et al., 1979). Moreover, little is known about the behaviour of gases at high pressure (i.e. most of the F and σ are obtained for low pressure confined inclusions). Chou et al. (1990) and Seitz et al. (1993, 1996) investigated the effect of pressure on the F and G factor (ratio between the F or G of the 2 species) for CH_4-N_2 and CH_4-CO_2 synthetic fluid inclusions mixtures. In both systems, a strong change in the F ratio is observed as a function of pressure up to 700 bars. However, no investigation has been performed at very high pressure (few hundreds MPa).

1.2 Research objectives: Quantitative analysis through LMR.

We have conducted an analytical study based on the combined use of LRM and ^{13}C-MAS NMR for a series of synthetic CO_2-CO bearing fluid inclusions.

The objective was to obtain a reliable calibration for the analysis of CO_2-CO bearing fluid inclusions by LMR, in order to derive F and G ratios for the CO-CO_2 mixture. Results are valid for ^{13}C isotopes but we tried to extend the results to ^{12}C species. Results will be discussed. Comparison with previous published data is difficult as the derived calibration is only valid for our LRM equipment (LabRam Jobin-Yvon). Application and discussion on the oxygen fugacity conditions during the experiments is also addressed. The $f(O_2)$ calculated using LRM fluid inclusion analyses is compared to the $f(O_2)$ value calculated through the H_2O dissolved in the glass. The relatively good agreement between the two methods suggests the reliability of our calibration.

2 Experimental and Analytical methods:

2.1 Experimental synthesis:

Synthetic Fe-free basaltic glasses in equilibrium with excess COH fluid phase were synthesized under high pressure high temperature using an Internally Heated Pressure Vessel (IHPV). The starting composition was prepared from a mixture of oxides (SiO_2, Al_2O_3 and MgO) and carbonates (Na_2CO_3 and $CaCO_3$). A two stage preparation was employed: 1) SiO_2, Al_2O_3, MgO and $CaCO_3$ were mixed together and held at 1050°C for few hours in order to dissociate the calcium carbonate (the resulting powder should be then CO_2-free); and 2) the Na_2CO_3 is added to complete the composition and is the source of CO_2 during the experiment.

The composition in wt.% is 54.8, 21.1, 8.1, 12.9 and 3.2 for SiO_2, Al_2O_3, MgO, CaO and Na_2O respectively. The CO_2 added to the composition through the sodium carbonate is at

1 wt.% level. The sodium carbonate source added is 100% ^{13}C-doped which is the only C species with a nuclear spin to be analysed by Solid-State MAS NMR.

Small amount of H_2O (between 0 and 1 wt.%) is added at the bottom of the platinum capsules. Starting composition is loaded on top of the water and the platinum capsule is sealed. Experiments are conducted in IHPV with run duration between 2 to 3 hours to ensure equilibrium is reached. The experimental conditions are 200 and 300 MPa for pressure, 1225 and 1250°C for temperature. The details of the experimental conditions for each sample are reported in Table 1.

Under those P,T conditions, the 1 wt.% $^{13}CO_2$ added to the staring composition is well above the solubility saturation level for basaltic compositions (Fine and Stolper, 1986; Pan et al., 1991; Dixon et al., 1995). Therefore, we expect the melt to be in equilibrium with an excess fluid phase in which C-species dominate.

The procedure to achieve the experimental conditions is described elsewhere (e.g., Scaillet et al., 1992) and can be summarized as follow. The IHPV is loaded at room temperature with a known partial pressure of pure H_2 ($P(H_2)$, see Table 1), Argon gas is then loaded up to roughly half the desired total pressure (P^{tot}) value (either 100 or 150 MPa). The temperature is then brought to the final value. Previous experiments have shown that under those P-T conditions the final estimated $P(H_2)$ is therefore equivalent to roughly two times the initial loaded $P(H_2)$. The final $P(H_2)$ experienced during the run are shown in Table 1. At run conditions, the hydrogen diffuses into the Pt capsule and acts as reducing agent for the loaded CO_2 according to the reaction in the fluid phase:

$$CO_2^{fl} + H_2^{fl} \leftrightarrow CO^{fl} + H_2O^m \qquad (5)$$

where *fl* stands for the gas in the fluid phase and *m* stands for the species in the melt phase. Further reduction will produce CH_4 as shown by Eq. (3).

The water produced during those reactions will mostly enter into the melt (H_2O^m) as the solubility level is very high compared to CO_2 and little water will be observed into the fluid inclusions (see Table 2). The range of $P(H_2)$ was chosen to 1) avoid graphite saturation and 2) minimize the presence of CH_4 (Eq. (3)). Although we mainly obtained a mixture of CO_2-CO in the fluid phase, CH_4 was still identified. No graphite was observed in the whole sample (glass and fluid inclusions as revealed by NMR analysis).

The sample is quenched to the ambient temperature by dropping the capsules into the cold part of the IHPV. During the quench, the fluid phase is mainly located at the top of the capsules; however a non-negligible part of the fluid phase will be entrapped as inclusions inside the glass.

Several chips from the recovered glasses were selected for micro-Raman and FTIR analyses. Remaining of the glass sample was then crushed for ^{13}C-MAS NMR analysis.

2.2 Confocal Micro-Raman:

LRM was used to characterize the fluid species inside the inclusions. The Raman system is a Jobin-Yvon Labram spectrometer (focal distance = 300 mm) equipped with a 1800 gratings/mm CCD detector. The light source is an Ar laser Innova 300-5W from Coherent© operating at 514.5 nm. The analyses were performed in confocal mode (hole = 500 μm, slit = 200 μm) so the contribution of the surrounding glass is limited and the inclusion contributes to the majority of the Raman scattering signal.

Spectrometer was set in the region of the CO_2-CO scattering between 1100 and 2200 cm^{-1}. Analyses were also done in the CH_4 region (2900 cm^{-1}) to check its presence. The spectral frequency position was measured with the emission lines of Ne- and Hg-lamps. The accuracy stays within ± 1 cm^{-1}.

We used a variable output laser power between 25 and 200 mW. The acquisition time on a given inclusion was typically between 10 and 120 sec.. We have tested the influence of laser power and acquisition time on two inclusions in KB16. No change in the ratio of the different species was observed with varying analysis conditions. The determined ratio standard deviation does not exceed 3% in value. All analytical conditions are reported in Appendix.

More than 10 different inclusions for KB3, 5, 8 and 16 were analyzed for the calibration of the Raman quantification factors.

For some inclusions (see Appendix), the LRM spectrum was acquired in oversaturation conditions of the detector for the main CO_2 peak. For example, in KB5-14 the $2\nu_2$ $^{12}CO_2$ resonance is not measured as it was above the saturation level of the CCD detector. The aim was to increase the intensity of the minor constituant peak, the $2\nu_2$ $^{13}CO_2$ resonance. For KB10 and 12, we analyzed 2 inclusions. Those samples were not included into the calibration. They are used as an independent verification for the reliability of our work in the $f(O_2)$ calculation.

2.3 Micro-FTIR analyses for glass water content:

Doubly polished plates were prepared from selected glass sections for micro-FTIR analyses in order to quantify the water content (H_2O^m). Near-IR spectra (between 4000

and 6000 cm^{-1}) were obtained for 100 μm spot size using a Continuμm microscope attached to a Nicolet 5700 Fourier transform infrared spectrometer. A KBr beamsplitter and MCT-B detector were used to collect 128 scans at a resolution of 4 cm^{-1}. The atmospheric contribution (in particular water) was reduced by enclosing the sample in a box purged with dry air for at least 20 minutes. Prior to sample acquisition, an instrumental background was subtracted.

Several spectra were taken on different location in the glass plate. A volatile-free FTIR spectrum was taken on a dry glass synthesized at 1300°C, 1 atm. and was subtracted to each volatile-bearing samples spectrum.

2.4 ^{13}C-MAS NMR:

^{13}C-MAS NMR spectra of the partially crushed samples were acquired on a 500 MHz Bruker Avance (11.7 T). A 4 mm CP/MAS "double bearing" probe was employed and the samples loaded in a ZrO_2 rotor with Teflon end-cap. Rotors were spun at 10 kHz. The measurements were made at the ^{13}C frequency (125.75 MHz). All spectra are referenced against TMS (Tetramethylsilane).

For all samples, ^{13}C-MAS NMR spectra were acquired with single $\pi/4$ excitation of 2 μs (SPE spectra). For both KB8 and 16, 13C-MAS NMR spectra were also acquired by using a rotor-synchronised spin-echo sequence ($\pi/2 - \tau - \pi - \tau -$ acq.) with a $\pi/2$ pulse of 4 μs and τ equal to one rotor period. In all cases, ^{1}H decoupling during acquisition (SPINAL64 scheme with a rf field of 60 kHz) was used to prevent from broadening of the ^{13}C lines due to heteronuclear interactions with protons (Laws et al., 2002). However, due to the very sharp signature of CO_2 and CO in the fluid phase and the presence of

protons only in the surrounding glass, the broadening effect is unlikely to occur., During the evolution time in the spin-echo sequence (τ), both CO_2 and CO may evolve differently; however it is unlikely it will produce a large difference on the quantification for this gaseous species especially for 1 rotor period (0.1 msec.) where the evolution is relatively small.

C-species can have long spin lattice relaxation times in silicate glasses (several minutes, Kohn et al., 1991). It is not the case in fluid phases where relaxation timescale are very short, we used several recycle time D1 (2, 20 sec., see Table 1 and Figure 2A) values to check the consistency in the response of the C-species.

The number of scans collected is relatively large because of the low CO_2 solubility in the melt and the small quantity of fluid inclusions (the most important part of the fluid escapes during the opening of the capsule). Thus, depending on D1 values, between 3k and 103k scans have been co-added.

3 Results:

3.1 Description of fluid inclusions:

Figure 1 shows typical fluid inclusions observed within the samples. Inclusions are disseminated but can be locally concentrated. The inclusions are entrapped during the quench in a glass matrix either clear in the case of KB16, KB8, KB10 and KB12 or cloudy in KB3 and 5. The cloudiness is due to the presence of crystals in the glass. The nature of the crystal is not fully known but we suggest it is unreacted material preserved during the quench. Due to the peraluminous character of the starting composition (21 wt.% Al_2O_3), we suppose the unreacted material are alumina or mullite crystals.

The inclusions are round-shaped and therefore considered as primary (Roedder, 1984) with sizes ranging from ~10 to 100 μm. Larger inclusions were seen but are very often pierced. The inclusions are clear and do not present either graphite lining or solid independent phase inside (Roedder, 1984).

3.2 Fluid inclusion spectrum analyses:

3.2.1 ^{13}C-MAS NMR spectra:

Figure 2A shows NMR spectra for KB3 (acquired with different recycle delay, D1 = 2 and 20 sec.) and KB5. Two major peaks are observed on the spectra: one located at 125 ppm and assigned to $^{13}CO_2$ and one located at 183.5 ppm and assigned to ^{13}CO (Kohn et al., 1991). No peak is observed at around 0 ppm which would reveal the presence of $^{13}CH_4$ (Ripmeester and Ratcliffe, 1988; Subramanian et al., 2000). The same observation is made for the other samples. There is a weak broad peak visible in KB5 between 160 and 175 ppm which is attributed to carbonate groups (CO_3^{2-}). CO_2 dissolves in basaltic melt only as CO_3^{2-} units (Blank and Brooker, 1994). The presence of such a broad signal is given by the molecular environment of CO_3^{2-} dissolved in the glass. On the other hand, the presence of CO_2 and CO can only be assumed to be entrapped into fluid inclusions and not dissolved in the glass.

Experiments were performed in water undersaturated conditions (i.e. most of the H_2O and H_2 will dissolve in the glass, Gaillard et al., 2003). If H is present, it will reduce CO_2 to form CH_4.

LRM suggests the presence of CH_4 in the fluid inclusion. However, the CH_4 concentration is estimated to be very small and therefore below the NMR detection limit (a few %).

The CO_2 molar fraction ($X(^{13}CO_2)$) is calculated using the ratio of the integrated area underneath the peaks at 125 and 180 ppm.

Using several D1 time does not modify the ratio of the C species (Table 1 and Figure 2A). In KB3, for D1 = 2 sec., the $X(^{13}CO_2)$ is equal to 0.728. $X(CO_2)$ for D1 = 20 sec. differs slightly and is equal to 0.770. The difference is probably within error and the standard deviation (0.029) between the 2 values will be used for the other samples measurements of $X(CO_2)$. In Table 1, we report 0.749 as the average of the 2 values. The same applies for the 2 NMR analytical conditions used for KB16 (SPE and spin-echo spectra). Only a slight difference is observed in between the $X(^{13}CO_2)$ values from 0.689 for SPE to 0.634 for spin-echo spectrum. The error bar reported for KB16 (± 0.038, Table 1) is probably the maximum error that we can observe. This value will be used later in the error propagation calculation for correcting the data by water activity. It should be mentioned that those values are not corrected for H_2O molar fraction ($X(H_2O)$) in the fluid phase (see section 4.3).

3.2.2 Confocal micro-Raman spectra:

Typical Raman spectra are reported in Figure 2B for several samples. The dashed line underneath corresponds to a typical baseline placed prior to the integration measurements.

Several peaks are observed. Two groups of peaks are located: 1) in the 1300 cm^{-1} region and is assigned to CO_2 molecules and 2) in 2100 cm^{-1} region and corresponds to CO molecules. However within each group several peaks are seen. For the CO molecules, 2 peaks are located at 2090 and 2137 cm^{-1} and are assigned to ^{13}CO and ^{12}CO respectively. The CO_2 in the fluid phase is represented by the Fermi diad (Wienecke et al., 1986) at ~1283, 1386 cm^{-1} for $^{12}CO_2$ and 1369, 1262 cm^{-1} for $^{13}CO_2$. Each individual resonance corresponds to the $2\nu_2$ and ν_1 respectively (Rosasco et al., 1975; Garrabos, 1980; Kerkhof and Olsen, 1990).

Additionally, we identified in KB16 (also identified in KB10 and 8) the CH_4 symmetric stretch (ν_1) at very low Raman shift value at 2900 cm^{-1} (usually ~2915 cm^{-1} as mentioned in Kerkhof, 1987; and Larsen et al., 1992). Because our samples are enriched in ^{13}C isotope, we suggest this peak to be attributed to $^{13}CH_4$. The intensity of the CH_4 peak is lower than CO peak and we regard this species as a minor diluted component. For KB12 (sample with the lowest $P(H_2)$), CH_4 is totally absent from the spectrum or below detection limit. The small proportion of CH_4 observed by LRM is in agreement with the NMR results which do not identify its presence.

The hot band near the Fermi diad of CO_2 are the result of two effects (Rosso and Bodnar, 1995; Dubessy et al., 1999; Chen et al., 2004): 1) the anharmonicity of the vibrational levels producing different energetic differences between two successive vibrational levels; and 2) the population of the excited vibrational levels increases with temperature. In Figure 2B, only one hot band is visible and observed at 1406 cm^{-1}. Other hot bands may be observed as we increase the temperature above 200°C.

Samples were supposed to exhibit 100% in ^{13}C, but the incomplete decarbonatation of $Ca^{12}CO_3$ in the starting powder suggests ^{12}C is still abundant and present as $^{12}CO_2$, ^{12}CO in the fluid inclusions.

The signature of each species was quantified either by measuring the height (H) or the area (A) of the peaks. A typical baseline is represented in Figure 2B (dashed line) underneath the Raman spectrum.

Results from the integrated areas and heights of the different peaks (CO_2 $2\nu_2$, ν_1 and CO for ^{13}C and ^{12}C) are reported in the Appendix for the different analyzed inclusions. Peak areas or height have been measured with the built-in functions in Origin© software. A and H are proportional 1) to the quantity of analyzed molecules (function of fluid density, composition, size and depth of the inclusion), 2) to the Raman analytical conditions. For a given inclusion, increasing the acquisition time will increase the precision of the measurement.

From the integrated areas and the peak heights of the different species within the fluid inclusions, we can therefore calculate 1) the enrichment in ^{13}C in each sample, 2) the fractionation $^{13}C/^{12}C$ if it exists, 3) calibrate Raman quantification factor (F and G) by combining the NMR and the Raman results for ^{13}C-species and thus 4) give an estimate of the molar fraction $X(^{13}CO_2)$ of each individual fluid inclusion which is used to calculate the $f(O_2)$ the samples experienced during the run in equilibrium with the fluid phase. We extended further our calibration method to ^{12}C-species. Raman quantification factor (F and G) and the $X(^{12}CO_2)$ are determined for ^{12}C-species by combining the ^{13}C-NMR results and the ^{12}C-species Raman results.

3.2.3 Water content in the glass matrix (H_2O^m): FTIR analyses.

The water content in the glass (H_2O^m) was determined by micro-FTIR measurements. Quantification of the H_2O^m is then used to estimate the $X(H_2O)^{fl}$ as well as the $f(O_2)$ (see section 4).

In Figure 3, we show the FTIR spectra obtained for the basaltic glass in the water vibration region (KB10 is not shown for clarity). Two main water species are identified. One vibration located at 4500 cm^{-1} is assigned to OH groups and one at 5200 cm^{-1} is assigned to the bending of H_2O in its molecular form (H_2O^{mol}), consistent with previous studies (e.g., Stolper, 1982a; Ihinger et al., 1994; King et al., 2002; Stuke et al., 2006). The H_2O^{mol} species are observed for samples with the highest water content whereas OH groups are always present which is in agreement with H_2O speciation models.

The H_2O^m is determined by quantifying the sum of each individual species (i.e., OH groups + H_2O^{mol}). We used the Beer-Lambert approximation (Morizet et al., 2002, 2007):

$$C_i = \frac{Abs_i \cdot 18.02}{\rho \cdot d \cdot \varepsilon} \qquad (6)$$

where C_i, the concentration of i-species, is a function of the integrated absorbance of the peak vibration (Abs_i) times the molecular mass of the water molecules (18.02, $g.mol^{-1}$) and divided by the product between the density (ρ, $g.L^{-1}$), the thickness of the sample (d, cm) and the integrated molar extinction coefficient for the considered specie (ε, $L.mol^{-1}.cm^{-2}$).

Reliable quantification can only be achieved if suitable values for ε are available. In order to be consistent, we have used for all samples the ε values derived by Stolper (1982a) and

valid for basaltic composition: 200 $L.mol^{-1}.cm^{-2}$ for OH groups and 300 $L.mol^{-1}.cm^{-2}$ for H_2O^{mol}. Vibration at 3550 cm^{-1} for total water was not used as the total peak could not be obtained, especially for high water content. A density value of 2537 $g.L^{-1}$ was used and determined from Lange and Carmichael (1987) glass density model. The spectra for each sample were normalised to 100 μm thick.

The calculated H_2O^m is indicated in Figure 3. The value is based on the FTIR measurements of at least 3 different spectra. The error on each value is calculated from the standard deviation analysis of the sum OH, H_2O^{mol} concentrations. For KB3, the OH signal is very weak. The H_2O^{tot} error reported in the Figure 3 is probably underestimated and may be closer to +/- 0.1 wt.% rather than +/- 0.01 wt.%.

4 Discussion:

4.1 Raman quantification factor (F, G) ratios for ^{13}C species:

From the Placzek's polarizability theory, a quantitative analysis of the species molar fraction can be achieved (Schrötter and Klöckner, 1979; Wopenka and Pasteris, 1986, 1987; Dubessy et al., 1989; Burke, 2001).

Applying Eq. (4) to our binary fluid system (CO_2-CO), the $X(CO_2)$ can be calculated using the peak area (A) or height (H):

$$X\left(CO_2\right)=\frac{\frac{A\left(CO_2\right)}{F\left(CO_2\right)}}{\frac{A\left(CO_2\right)}{F\left(CO_2\right)}+\frac{A\left(CO\right)}{F\left(CO\right)}} \qquad (7)$$

$$X\left(CO_2\right)=\frac{\frac{H\left(CO_2\right)}{G\left(CO_2\right)}}{\frac{H\left(CO_2\right)}{G\left(CO_2\right)}+\frac{H\left(CO\right)}{G\left(CO\right)}} \qquad (8)$$

F and G are the Raman quantification factors used with the area and the height of the peaks respectively. Both values are of interest and provide complementary information. G-factor value has been constrained for other binary gas mixtures. Seitz et al. (1993, 1996) derived the G- and F- factor for CH_4-N_2 and CH_4-CO_2 gas mixture. For example, the G-factor between CH_4 and CO_2 shows more variability compared to the F-factor as a function of pressure. Such difference for CH_4-CO_2 could be the result of modified molecular interactions upon pressure inducing a peak line broadening.

Eq. (7) and (8) are linear. Area and height should be measuring the same quantities. In Figure 4, we have reported the peaks areas (A_i) versus the peak heights (H_i, see Appendix for data) for all observed species and resonance (CO_2 $2\nu_2$, ν_1 and CO for ^{13}C and ^{12}C) which were measured from all inclusions by LRM. There is a clear linear trend ($A_i = 4.70\ H_i$) relating the height and the area of a given resonance which is consistent with the linear aspect character of Eq. (7) and (8).

We consider a mixture between CO_2 and CO in the fluid phase. We make the assumption that the small amount of CH_4 does not intervene in the $X(CO_2)$ calculation. The Raman scattering coefficient for CH_4 is 8 times higher than for CO_2 or CO (Seitz et al., 1996; Burke, 2001). In KB16, the area measured for the presence of CH_4 is roughly equivalent to the area measured for CO. We estimated that CH_4 would only represent less than 5 % ($X(CH_4) < 0.05$) in the fluid phase which is probably within the error of the Raman measurements.

With CO_2 and CO, Eq. (4) and (5) can be rearranged and can be expressed as a function of the F- and G-factors:

$$\left(1-X\left(CO_2\right)\right)\times A\left(CO_2\right)=X\left(CO_2\right)\times A\left(CO\right)\times\frac{F\left(CO_2\right)}{F\left(CO\right)} \qquad (9)$$

$$\left(1-X\left(CO_2\right)\right)\times H\left(CO_2\right)=X\left(CO_2\right)\times H\left(CO\right)\times\frac{G\left(CO_2\right)}{G\left(CO\right)} \qquad (10)$$

We obtain a linear relation between A (or H) and the F (or G) ratio passing through zero. Eq. (9) and (10) can be applied to either C isotope but we first consider the ^{13}C for which NMR data is available. $A(CO_2)$ stands for the area of the CO_2 peak which is either the $2\nu_2$ or ν_1 resonance. We considered the resonance of the CO_2 diad individually, although, Dubessy et al. (1989) suggested using the sum of the peak areas for quantification. Seitz et al. (1996) on the other hand concluded that it was more reliable to use the $2\nu_2$ resonance instead of the peaks sum. We will see in fact that each resonance may be used without significant difficulties.

Application of Eq. (9) and (10) is represented in Figure 5. We use the values obtained from NMR as an input for the $X(^{13}CO_2{}^{NMR})$ and combined it with either the area of Raman peaks (Figure 5A and 5B) or the height of Raman peaks (Figure 5C and 5D). In order to be consistent with the NMR results, we only used the Raman information for the ^{13}C isotope..

Although, we obtain a good linear correlation (dashed line) with 95% confidence interval (dotted lines) for the calibrations of the F ratios using the area of the peaks (Figure 5A and 5B) a slight variability may be observed. We do not preclude from compositional

heterogeneity in the fluid inclusions. Slight change in the fluid inclusion composition is only visible through Raman analysis but is averaged out with the NMR bulk method. The height of the peak gives a good correlation when using the $2\nu_2$ resonance (Figure 5C and 5D). We obtain an $F(2\nu_2\ ^{13}CO_2)/F(^{13}CO) = 1.956 \pm 0.028$. Calibration of the G-factor provides similar results with $G(2\nu_2\ ^{13}CO_2)/F(^{13}CO) = 1.809 \pm 0.035$. This is in agreement with the fact that the area and height of the peaks should be measuring the same quantity. Up to now, no data are available for the calibration of the ν_1 CO_2 peak quantification factor. We find a value $F(\nu_1\ ^{13}CO_2)/F(^{13}CO) = 0.526 \pm 0.014$. Using the height of the peak, we calibrated the G ratio for ν_1 resonance of $^{13}CO_2$. In Figure 5D, it seems there are multiple correlations. We can separate the dataset in 2 parts: the first represented by KB16 and the second represented by the other samples, KB3, 5 and 8. Two trends are identified. For KB16, the G factor is roughly 0.3 whereas for KB3, 5 and 8, the G factor is around 0.5. The main difference in between the samples is the ^{13}C enrichment which is different. KB16 has roughly 80% in ^{13}C isotopes. KB3, 5 and 8 are enriched at a lower level (~40%). The multiple trends aspect only concerns the ν_1 calibration and this behaviour is not observed for the $2\nu_2$. The use of the ν_1 resonance height may not be suitable for relevant calibration of randomly enriched samples. The shape of the ν_1 resonance peak is not changing linearly with the ^{13}C enrichment of the samples.

4.2 Raman quantification factor applied for ^{12}C species:

Calibration results obtained for ^{13}C-species are extended to ^{12}C-species to test if whether or not CO_2 and CO molecules in both isotopes possess the same Raman cross-sections (i.e. F or G ratio for $2\nu_2\ ^{12}CO_2$ / ^{12}CO are similar). In other words, we test the assumption

that ^{13}C and ^{12}C species do not fractionate in the fluid phase and enter the melt phase indifferently. We regard the reaction $CO_2 \leftrightarrow CO + ½ O_2$ as equivalent in between the isotopes on a thermodynamic point of view.

Using the $X(^{13}CO_2)$ measured from NMR, combining it with the integrated area and the height of the $2\nu_2$ $^{12}CO_2$ and ^{12}CO, we have derived the F and G ratio for the ^{12}C species which is represented in Figure 6A and 6B. We only used this approach for $2\nu_2$ resonance for clarity as we suggested ν_1 not to be reliable enough for calibration as seen in Figure 5D. Although we take the $X(^{13}CO_2)$ from NMR, if a significant difference would exist in between the two isotopes then several trends will be expected. For example in Figure 5D, we observe 2 different trends for the calibration of the G factor of the ν_1 resonance. The 2 trends are likely to be explained by the different enrichment in ^{13}C isotope: KB16 is more enriched in ^{13}C (~80%) than the other samples (~40%).

Values derived from the linear fit are 1.856 ± 0.057 and 1.756 ± 0.054 for F and G factor respectively for ^{12}C isotope. Those values are in the same order as for the calibration obtained for ^{13}C species. The errors on the values are larger than for ^{13}C species G and F factors. The data points for KB3 in particular show a large scatter compared to the other samples. Thus, as KB3 is included in the fit, it represents the major source of error in the final values. Removing KB3 data points would probably increase the obtained value for F and G factors. A slight heterogeneity in the KB3 fluid inclusions compositions may be responsible for the large scatter.

The F ratio given by Wopenka and Pasteris (1987) for the $2\nu_2$ $^{12}CO_2$ and ^{12}CO is reported for comparison (1.55 corresponding to 1.52 and 0.98 for $2\nu_2$ $^{12}CO_2$ and ^{12}CO Raman scattering cross-section).

The F ratios value obtained from linear regression in Figure 6 ($2\nu_2$ $^{13}CO_2$ vs. ^{13}CO) is only slightly different from the one established by Wopenka and Pasteris (1987) determined for a RAMANOR U-1000 spectrometer.

The difference in between the calibration values may be due to either different Raman efficiency coefficient value (ζ) or a true effect of the fluid inclusions trapping conditions. Synthetic fluid inclusions in Wopenka and Pasteris (1987) were formed at less than 1.5 MPa. Although we did not measure the pressure inside the inclusions, it is likely that the pressure inside our fluid inclusions is higher. The different inclusion pressure could have a possible effect on the quantification factor.

The supposed change for F with pressure has implications for the quantification of high pressure fluid species through LRM. If one needs to determine the molar fraction of a gas species entrapped at high pressure then a proper calibration needs to be done for the quantification factor as the reported value for low pressure fluid inclusions may not be suitable for high pressure domain. Yet, it is currently unknown what behaviour the F and G factor could adopt at very high pressure. Using non suitable value for high pressure fluids may therefore induce a significant error on the determination of the gas mixture composition and thus on the molar fractions calculations.

Because we obtain similar value for the F and G factors for the 2 different isotopes, we conclude that our analytical approach (combining NMR and LRM analysis to constrain the Raman quantification factor) is adequate. Moreover, we also suggest that ^{12}C and ^{13}C species have comparable behaviour for Raman scattering. Thus, both isotopes can be quantified through LRM with the same F or G factor.

4.3 CO_2 molar fraction recalculated from LRM and correction for H_2O content in the fluid phase:

The calibration has been performed considering only CO_2 and CO are present in the fluid phase and neglecting the presence of CH_4 as C-species. However, CO_2 and CO species should be in thermodynamic equilibrium with H_2O in the fluid phase as H_2O is present in the melt. We estimated the H_2O molar fraction in the fluid phase ($X(H_2O)$) according to Eq. (11):

$$X\left(H_2O\right)=\frac{f\left(H_2O\right)}{P_{tot}\cdot\phi\left(H_2O\right)} \qquad (11)$$

where $f(H_2O)$ stands for the H_2O fugacity; P_{tot} is the total pressure of the experiment; ϕ is the H_2O fugacity coefficient. The $f(H_2O)$ was estimated from the model of Dixon et al. (1995) which relates the H_2O solubility in the melt to the H_2O fugacity in the fluid. H_2O fugacity coefficient is determined from the equation of state given in Shi and Saxena (1992). The results on the $X(H_2O)$ are reported in Table 2. Values oscillates from almost 0 for KB3 and up to ~20% for KB12. Although most of the calculated values are below 10% for the other samples. The error on the $X(H_2O)$ was calculated considering an error of +/-10 bars on the determination of the $f(H_2O)$.

Using the calibration of G and F factors obtained for the $2\nu_2$ CO_2 resonance (see Figure 5 and 6), we have recalculated the $X(^{13}CO_2)$ and $X(^{12}CO_2)$ uncorrected for $X(H_2O)$. Results are given in Table 2. Each value represents the average and the standard deviation for $X(CO_2)$ obtained from all the fluid inclusions analyzed by LRM.

The $X(CO_2)$ in the fluid phase has been recalculated accounting for the amount of H_2O present in the fluid phase. According to mass balance and considering ^{12}C and ^{13}C isotopes do not produce significant fractionation, we have:

$$X\left(H_2O\right)+X\left(CO_2\right)+X\left(CO\right)=1 \qquad (12)$$

Correction on the $X(CO_2)$ was done according to the following equation:

$$X\left(CO_2\right)_{corrected}=\frac{1-X\left(H_2O\right)}{\alpha+1} \qquad (13)$$

where $\alpha = X(CO)/X(CO_2)$ determined from either NMR or LRM prior correction.

The $X(CO_2)$ corrected value is also reported in Table 2. For a low $X(H_2O)$, the $X(CO_2)$ corrected value does not significantly change from the uncorrected one. In KB3, $X(CO_2)$ changes from 0.769 to 0.766 for uncorrected and corrected value respectively. It is not the case for KB12 for which the $X(CO_2)$ is decreased from ~0.93 to ~0.75 between uncorrected and corrected value.

In Figure 7, the corrected $X(CO_2)$ determined by LRM are plotted against the corrected $X(^{13}CO_2)$ measured by NMR. The 1:1 line is also reported for comparison. The plot is presented in the range of molar fraction of interest (0.5 to 0.9).

The obtained calibration is satisfactory for most of the samples as the $X(CO_2)$ LRM reproduces well the $X(^{13}CO_2)$ NMR. ^{13}C species abundances are reproduced precisely by the produced calibration.

Reproducing the $X(^{12}CO_2)$ by LRM appears more difficult especially for KB16 (~0.68 for $X(^{12}CO_2)$ by LRM versus ~0.61 by NMR). One source of disagreement can potentially be the different enrichment in ^{13}C observed in KB16; however this point would have to be confirmed with further fluid inclusion analyses on different $^{13}C/^{12}C$ ratios.

4.4 Oxygen fugacity calculation from H_2O and CO_2 equilibrium reactions:

In the fluid phase, CO_2, CO and O_2 are in thermodynamic equilibrium according to Eq. (2). Using the thermodynamic formalism described by Shi and Saxena (1992), we have calculated the $f(O_2)$ within each sample. The Eq. (2) equilibrium constant ($K(CO_2)$) is related the $X(CO_2)$ and X(CO) measured in the fluid according to the relation:

$$K\left(CO_2\right)=\frac{X\left(CO\right)\phi\left(CO\right)\cdot f\left(O_2\right)^{\frac{1}{2}}}{X\left(CO_2\right)\phi\left(CO_2\right)} \qquad (14)$$

where ϕ is the fugacity coefficient determined from equation of state and K from the thermodynamic database given in Shi and Saxena (1992).

The redox state of the fluid ($f(O_2)$) is calculated following two methods. The first one is based on the CO_2-CO-O_2 equilibrium from fluid inclusion data and the second one on the H_2O-H_2-O_2 equilibrium using $f(H_2)$ known from experimental conditions and $f(H_2O)$ derived from solubility of water in the melt at experimental P and T conditions. As stated before, H_2O^m is in equilibrium with H_2O^{fl}, which implies that $a(H_2O)^{fl} = a(H_2O)^m$ or $f(H_2O)^{fl} = f(H_2O)^m$. If the redox state ($f(O_2)$) is controlled by H_2 fugacity, according to Eq. (1), the relationship between different gas fugacity is the following:

$$K\left(H_2O\right)=\frac{f\left(H_2O\right)}{f\left(H_2\right)\cdot f\left(O_2\right)^{\frac{1}{2}}} \qquad (15)$$

where *f* represents the fugacity of the different species. $K(H_2O)$ is calculated from thermodynamic data in Shi and Saxena (1992). The $f(H_2)$ are experimentally applied values listed in Table 1.

Results are given in Table 3 listing the log $f(O_2)$ calculated with the two different methods and plotted in Figure 8. We choose to take the average of the log $f(O_2)$ (column 6) as representative of the LRM fluid inclusion analyses. The standard deviation on the calculated log $f(O_2)$ values is also represented. We only used the $X(CO_2)$-X(CO) values corrected for $X(H_2O)$ and shown in Table 2 to calculate the log $f(O_2)$. However, calculation with uncorrected $X(CO_2)$-X(CO) values changes the log $f(O_2)$ by only 0.01 log unit.

We observe in Figure 8 a large disagreement between the two calculation methods for KB3. This discrepancy may be explained by the remarkably low water content in KB3. H_2O^m estimation by FTIR is therefore more difficult and subject to very large error. The solubility of H_2O in silicate melt is a non linear function of $f(H_2O)$. For 0.27 wt.% H_2O^m we found a $f(H_2O)$ = 10 bars but owing to the associated analytical error of H_2O^m determination, we can not exclude this value to be 2 to 3 times higher which would change the log $f(O_2)$ by almost 1 unit.

Moreover such a value (log $f(O_2)$ ~-13 corresponds to extremely reducing conditions well below the graphite saturation. Those reducing conditions would induce a change in the appearance of the sample which should be totally blackened by the graphite crystals. The ^{13}C-MAS NMR would also have revealed the presence of very reducing species such as SiC or even AlC groups. This is not the case in the spectra (NMR or LRM).

The NMR results on the $X(CO_2)$ cannot be challenged as it is a more quantitative method than the FTIR. We suggest the H_2O^m method to calculate the $f(O_2)$ is less reliable for our glasses with low water content in regard of 1) the possible large error on the FTIR

measurements at low H_2O^m and 2) the corresponding large uncertainty on the fugacity estimate.

Another possibility is the departure from 1:1 line. It appears there is also an offset of 0.5 to 1.0 log unit for KB5 and KB8 respectively. Either it represents the absolute error on the log $f(O_2)$ calculation or one of the two method is not calculating the real log $f(O_2)$ at equilibrium.

For example, compositional changes can occur during quenching either in the fluid phase or the melt phase (Zhang et al., 1995; Morizet et al., 2001). Thermodynamic calculations are performed at run temperature, however the fluid inclusion spectroscopic measurements are conducted at room temperature. Therefore, the $X(CO_2)$ measured may not be entirely representative of the high temperature fluid composition. This hypothesis could only be tested with in-situ measurements.

On the other hand, for KB16, 10 and 12 we obtain an excellent agreement in between the two methods. KB10 and 12 were not included into the LRM calibration but were used as an independent test. The fact that KB10 and KB12 show an excellent correlation is a very strong witness for the reliability of the Raman quantification factor (F and G) calibration presented in this work.

5 Summary:

Determining the fluid inclusion composition relies on micro-analytical techniques such as LRM. LRM requires a relevant calibration for measuring the gas molar fraction within the fluid inclusions.

We have combined LRM and ^{13}C-MAS NMR analyses to produce a calibration for CO_2-CO gas mixture entrapped in synthetic fluid inclusions quenched from high temperature (1200-1250°C) and high pressure (2-3 kbars) experiments. The applied method with the use of NMR measurement has the major advantage to be independent of fluid density and is only function of fluid composition.

First, the calibration was applied to ^{13}C species. We have determined the F and G factors for $^{13}CO_2$ and ^{13}CO. From the CO_2 Fermi diad, we obtain a well defined unique linear trend when using the $2\nu_2$ $^{13}CO_2$ resonance whereas the use of the ν_1 resonance produce strange behaviour. We suggest that only the use of the $2\nu_2$ CO_2 resonance is suitable for determining the fluid composition in CO_2-CO mixture.

Second, considering ^{12}C and ^{13}C isotopes behave similarly, we have extended our calibration procedure with $^{12}CO_2$-^{12}CO species identified in the fluid inclusion and in equilibrium with ^{13}C species. We found values for F and G factors which are close to ^{13}C species F and G values. It implies that 1) ^{12}C and ^{13}C species are not strongly fractionated in the fluid phase and may be considered almost equally on a thermodynamic point of view, 2) Although the chosen approach is likely to be more robust for ^{13}C than for ^{12}C species, our calibration may be applied to both isotopes indifferently.

The observed values for F and G are different from previously published value for F and G. The difference may be the result of the 1) different entrapment pressure or 2) change in the Raman efficiency coefficient. Most of the reported fluid composition calibrations have dealt with low pressure synthetic inclusions. Up to now, no data for F and G factors are available for high pressure domain and this point needs to be investigated further.

$X(CO_2)$ has been recalculated according to the calibration results, it was then used to calculate the log $f(O_2)$ in the fluid phase. The calibration has also been tested using 2 independent samples which were not used in the calibration process. There is an excellent agreement between the log $f(O_2)$ calculated for those samples from fluid inclusions analyses and from water content within the melt.

A reasonable agreement is observed between the log $f(O_2)$ calculated from 1) the fluid inclusions analyses and 2) H_2O dissolved in the melt. However, at low H_2O content, there is a strong departure of the log $f(O_2)$ from the 1:1 line suggesting that log $f(O_2)$ calculation method from H_2O dissolved in the melt may not be suitable under these conditions. Thus, fluid inclusions analyses may be considered as an alternative approach for determining the log $f(O_2)$ in dry or nearly dry conditions.

Alternatively, a change in the fluid phase composition during quenching could explain this disagreement. However, only in-situ measurements of the fluid phase composition may be able to test this hypothesis.

Acknowledgements:

The authors are grateful to the University of Orléans, University of Nantes, the CNRS and INSU for their financial support and access to analytical facilities. We also thank Dr. R. Champallier and Mr. E. Lemenn for their technical help. We also would like to thank Prof. J. Dubessy and an anonimous reviewer for the constructive and helpful reviews.

Reference list:

Andersen, T., and Neumann, E.R., 2001. Fluid inclusions in mantle xenoliths. Lithos 55, 301-320.

Arculus, R.J., 1985. Oxidation status of the mantle: Past and present. Annual Review of Earth and Planetary Science 13, 75-95.

Beeskow, B., Rankin, A.H., Murphy, P.J., Treloar, P.J., 2005. Mixed CH_4-CO_2 fluid inclusions in quartz from the South Wales Coalfield as suitable natural calibration standards for microthermometry and Raman spectroscopy. Chemical Geology 223, 3-15.

Bergman, S.S., and Dubessy, J., 1984. CO_2-CO fluid inclusions in a composite peridotite xenolith: implications for upper mantle oxygen fugacity. Contribution to Mineralogy and Petrology 85, 1-13.

Bezos, A., and Humler, E., 2005. The $Fe^{3+}/\Sigma Fe$ ratio of MORB glasses and their implications for mantle melting. Geochimica Cosmochimica Acta 69, 711-725.

Blank, J.G., and Brooker, R.A., 1994. Experimental studies of carbon dioxide in silicate melts: solubility, speciation and stable carbon isotope behaviour. In: Carroll, M.R., Holloway, J.R. (Eds.), Volatiles in magmas. Review in mineralogy. Mineralogical Society of America, Washington, DC, 30, pp 157-186.

Boiron, M.-C., and Dubessy, J., 1994. Determination of fluid inclusion composition: microanalytical techniques. In: De Vivo, B., Frezzotti, M.L. (Eds.), Fluid Inclusions in minerals: Methods and Applications. Pontignano, Siena, pp 45-71, Short Course of the IMA Working Group 'Inclusions in Minerals'.

Burke, E.A.J., 2001. Raman microspectrometry of fluid inclusions. Lithos 55, 139-158.

Chen, J., Zheng, H., Xiao, W., Zeng, Y., Weng, K., 2004. Raman spectroscopic study of CO_2-NaCl-H_2O mixtures in synthetic fluid inclusions at high temperature. Geochimica Cosmochimica Acta 68, 1355-1360.

Chou, I.-M., Pasteris, J.D., Seitz, J.C., 1990. High density volatiles in the system C-O-H-N for the calibration of a laser Raman microprobe. Geochimica Cosmochimica Acta 54, 535-543.

Dereppe, J.-M., Pironon, J., Moreaux, C., 1994. Characterization of the composition of fluid inclusions in minerals by ^{1}H NMR. American Mineralogist 79, 712-718.

Dhamelincourt, P., Bény, J.-M., Dubessy, J., Poty, B., 1979. Analyse d'inclusions fluides à la microsonde MOLE à effet Raman. Bulletin de Minéralogie 102, 600-610.

Dixon, J.E., Stolper, E.M., Holloway, J.R., 1995. An experimental study of water and carbon dioxide solubilities in Mid-Ocean Ridge Basaltic liquids. Part I: Calibration and solubility models. Journal of Petrology 36, 1607-1631.

Dixon, J.E., 1997. Degassing of alkalic basalts. American Mineralogist 82, 368-378.

Dubessy, J., Poty, B., Ramboz, C., 1989. Advances in C-O-H-N-S fluid geochemistry based on micro-Raman spectrometric analysis of fluid inclusions. European Journal of Mineralogy 1, 517-534.

Dubessy, J., Moissette, A., Bakker, R.J., Frantz, J.D., Zhang, Y.-G., 1999. High temperature Raman spectroscopic study of H_2O-CO_2-CH_4 mixtures in synthetic fluid inclusions: first insights on molecular interactions and analytical implications. European Journal of Mineralogy 11, 23-32.

Fine, G., Stolper, E., 1986. Dissolved carbon dioxide in basaltic glasses: concentrations and speciation. Earth and Planetary Science Letters 76, 263-278.

Frezzotti, M.L., Peccerillo, A., 2007. Diamond-bearing COHS fluids in the mantle beneath Hawaii. Earth and Planetary Science Letters 262, 273-283.

Gaillard, F., Schmidt, B., Mac Cammon, C., Mackwell, S., 2003. Rate of hydrogen-iron redox exchange in silicate melts and glasses. Geochimica Cosmochimica Acta 67, 2427-2441.

Garrabos, Y., Tufev, R., Le Neindre, B., Zalczer, G., Beysens, D., 1980. Rayleigh and Raman scattering near the critical point of carbon dioxide. Journal of Chemical Physics 72, 4637-4651.

Gerlach, T.M., Graeber, E.J., 1985. Volatile budget of Kilauea volcano. Nature 313, 273-277.

Günther, D., Audétat, A., Frischknecht, R., Heinrich, C.A., 1998. Quantitative analysis of major, minor and trace elements in fluid inclusions using laser ablation-inductively coupled plasma mass spectrometry. Journal of Analytical Atomic Spectrometry 13, 263-270.

Holloway, J. R., 1987. Igneous fluids. In: Carmichael, I.S.E., Eugster, H.P. (Eds.) Thermodynamic Modelling of Geological Materials: Minerals, Fluids and Melts. (Review in mineralogy) Mineral. Soc. Am., Washington, DC, 17, pp 211-233.

Ihinger, P.D., Hervig, R.L., McMillan, P.F., 1994. Analytical methods for volatiles in glasses. In: Carroll, M.R., Holloway, J.R. (Eds.) Volatiles in magmas. (Review in mineralogy) Mineral. Soc. Am., Washington, DC, 30, pp 67-121.

Jambon, A., 1994. Earth degassing and large-scale geochemical cycling of volatile elements. In: Carroll, M.R., Holloway, J.R. (Eds.) Volatiles in magmas. (Review in mineralogy) Mineral. Soc. Am., Washington, DC, 30, pp 479-517.

Kadik, A., Pineau, F., Litvin, Y., Jendrzejewski, N., Martinez, I., Javoy, M., 2004. Formation of Carbon and Hydrogen species in magmas at low oxygen fugacity. Journal of Petrology 45, 1297-1310.

Kerkhof, A.M. van den, 1988a. Phase transitions and molar volumes of CO_2-CH_4-N_2 inclusions. Bulletin de Minéralogie 111, 257-266.

Kerkhof, A.M. van den, Kisch, H.J., 1993. CH_4-rich inclusions from quartz veins in the Valley-and-Ridge province and the anthracite fields of the Pennsylvania Appalachians – reply. American Mineralogist 78, 220-224.

King, P.L., Vennemann, T.W., Holloway, J.R., Hervig, R.L., Lowenstern, J.B., Forneris, J.F., 2002. Analytical techniques for volatiles: A case study using intermediate (andesitic) glasses. American Mineralogist 87, 1077-1089.

Kohn, S.C., Brooker, R.A., Dupree, R., 1991. ^{13}C MAS NMR: A method for studying CO_2 speciation in glasses. Geochimica and Cosmochimica Acta 55, 3879-3884.

Kress, V.C., Carmichael, I.S.E., 1991. The compressibility of silicate liquids containing Fe_2O_3 and the effect of composition, temperature, oxygen fugacity and pressure on their redox states. Contribution to Mineralogy and Petrology 108, 82-92.

Lange, R.A., Carmichael, I.S.E., 1987. Densities of Na_2O-K_2O-CaO-MgO-FeO-Fe_2O_3-Al_2O_3-TiO_2-SiO_2 liquids: new measurements and derived partial molar properties. Geochimica Cosmochimica Acta 53, 2195-2204.

Lee, S.K., Stebbins, J.F., 2003. The distribution of sodium ions in aluminosilicate glasses: A high-field Na-23 MAS and 3Q MAS NMR study. Geochimica Cosmochimica Acta 67, 1699-1709.

Liu, W., Fei, P.X., 2006. Methane-rich fluid inclusions from ophiolitic dunite and post-collisional mafic-ultramafic intrusion: The mantle dynamics underneath the Palaeo-Asian Ocean through to the post-collisional period. Earth and Planetary Science Letters 242, 286-301.

McMillan, P., 1984. Structural studies of silicate glasses and melts – applications and limitations of Raman spectroscopy. American Mineralogist 69, 622-644.

Morizet, Y., Kohn, S.C., Brooker, R.A., 2001. Annealing experiments on CO_2-bearing jadeite glass: an insight into the true temperature dependence of CO_2 speciation in silicate melts. Mineralogical Magazine 65, 701-707.

Morizet, Y., Brooker, R.A., Kohn, S.C., 2002. CO_2 in haplo-phonolite Melt: Solubility, speciation and carbonate complexation. Geochimica Cosmochimica Acta 66, 1809-1820.

Morizet, Y., Nichols, A.R.L., Kohn, S.C., Brooker, R.A., Dingwell, D.B., 2007. The influence of H_2O and CO_2 on the glass transition temperature: Insights into the effects of volatiles on magma viscosity. European Journal of Mineralogy 19, 657-669.

Neuville, D.R., Cormier, L., Massiot, D., 2006. Al coordination and speciation in calcium aluminosilicate glasses: Effects of composition determined by ^{27}Al MQ-MAS NMR and Raman spectroscopy. Chemical Geology 229, 173-185.

Pasteris, J.D., Wopenka, B., Seitz, J.C., 1988. Practical aspects of quantitative laser Raman microprobe spectroscopy for the study of fluid inclusions. Geochimica and Cosmochimica Acta 52, 979-988.

Pan, V., Holloway, J.R., Hervig, R., 1991. The pressure and temperature dependence of carbon dioxide solubility in tholeiitic basalt melts. Geochimica and Cosmochimica Acta 55, 1587-1595.

Pawley, A.R., Holloway, J.R., McMillan, P.F., 1992. The effect of oxygen fugacity on the solubility of carbon-oxygen fluids in basaltic melt. Earth and Planetary Science Letters 110, 213-225.

Ripmeester, J.A., Ratcliffe, C.I., 1988. Low-temperature cross-polarisation/magic angle spinning ^{13}C NMR of solid methane hydrates: structure, cage occupancy, and hydration number. Journal of Physical Chemistry 92, 337-339.

Roedder, E., 1984. Fluid inclusions. Rev. Mineral. 12, 644 pp.

Roedder, E., 1990. Fluid inclusion analysis – prologue and epilogue. Geochimica Cosmochimica Acta 54, 495-507.

Rosasco, G.J., Roedder, E., Simmons, J.H., 1975. Laser-excited Raman spectroscopy for non-destructive partial analysis of individual phases in fluid inclusions in minerals. Science 190, 557-560.

Rosso, K.M., Bodnar, R.J., 1995. Microthermometric and Raman spectroscopic detection limits of CO_2 in fluid inclusions and the Raman spectroscopic characterization of CO_2. Geochimica Cosmochimica Acta 59, 3961-3975.

Scaillet, B., Pichavant, M., Roux, J., Humbert, G., Lefèvre, A., 1992). Improvements of the Shaw membrane technique for measurement and control of fH_2 at high temperatures and pressures. American Mineralogist 77, 647-655.

Schrötter, H.W., Klöckner, H.W., 1979. Raman scattering cross-sections in gases and liquids. Springer-Verlag, Berlin, pp. 123-166.

Seitz, J.C., Pasteris, J.D., Chou, I-M., 1993. Raman spectroscopic characterization of gas mixtures: II. Quantitative composition and pressure determination of CH_4, N_2, and their mixture. American Journal of Science 293, 297-321.

Seitz, J.C., Pasteris, J.D., Chou, I-M., 1996. Raman spectroscopic characterization of gas mixtures: II. Quantitative composition and pressure determination of the CO_2-CH_4 system. American Journal of Science 296, 577-600.

Shepherd, T.J., Ayora, C., Cendón, D.I., Chenery, S.R., Moissette, A., 1998. Quantitative solute analysis of single fluid inclusions in halite by LA-ICP-MS and cryo-SEM-EDS: complementary microbeam techniques. European Journal of Mineralogy 10, 1097-1108.

Sherriff, B.L., Grundy, H.D., Hartman, J.S., 1987. Analysis of fluid inclusions using nuclear magnetic resonance. Geochimica Cosmochimica Acta 51, 2233-2235.

Shi, P., Saxena, S.K., 1992. Thermodynamic modeling of C-H-O-S fluid model. American Mineralogist 77, 1038-1049.

Stalder, R., Foley, S.F., Brey, G.P., Horn, I., 1998. Mineral-aqueous fluid partitioning of trace elements at 900-1200°C and 3.0-5.7 GPa: New experimental data for garnet, clinopyroxene, and rutile, and implications for mantle metasomatism. Geochimica Cosmochimica Acta 62, 1781-1801.

Stolper, E.M., 1982a. Water in silicate glasses: an infrared spectroscopic study. Contribution to Mineralogy and Petrology 81, 1-17.

Stuke, A., Behrens, H., Schmidt, B.C., Dupree, R., 2006. H_2O speciation in float glass and soda lime glass. Chemical Geology 229, 64-77.

Subramanian, S., Kini, R.A., Dec, S.F., Sloan, E.D., 2000. Evidence of structure II hydrate formation from methane + ethane mixtures. Chemical Engineering Science 55, 1981-1999.

Symonds, R.B., Rose, W.I., Bluth, G.J.S., Gerlach, T.M., 1994. Volcanic-gas studies: Methods, Results and Applications. In: Carroll M.R., Holloway J.R. (Eds.) Volatiles in magmas. (Review in mineralogy) Mineral. Soc. Am., Washington, DC, 30, pp 1-66.

Wienecke, P., Finsterhölzl, H., Schrötter, H.W., Brandmüller, J., 1986. Raman spectra of carbon dioxide and its isotopic variants in the Fermi resonance region. Part IV: Temperature dependence on Q-branch intensities from 300K to 650K. Applied Spectroscopy 40, 70-75

Wopenka, B., Pasteris, J.D., 1986. Limitations to quantitative analysis of fluid inclusions in geological samples by laser Raman microprobe spectroscopy. Applied Spectroscopy 40, 144-151.

Wopenka, B., Pasteris, J.D., 1987. Raman intensities and detection limits of geochemically relevant gas mixtures for a laser Raman microprobe. Analytical Chemistry 59, 2165-2170.

Wopenka, B., Pasteris, J.D., Freeman, J.J., 1990. Analysis of fluid inclusions by Fourier transform infrared and Raman microspectrometry. Geochimica Cosmochimica Acta 54, 519-533.

Zhang, Y., Stolper, E.M., Ihinger, P.D., 1995. Kinetics of the reaction $H_2O + O = 2OH$ in rhyolitic and albitic glasses: Preliminary results. American Mineralogist 80, 593-612.

Figure caption:

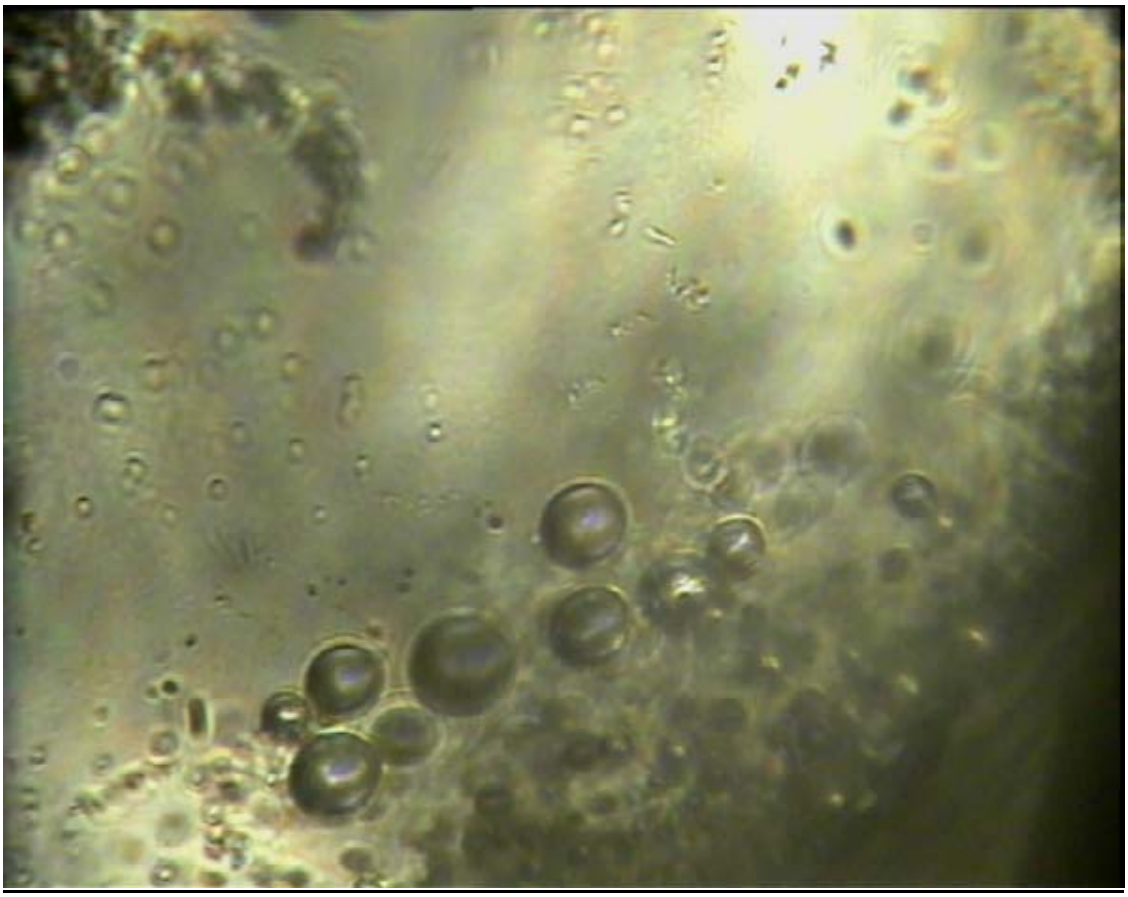

Figure 1: Fluid inclusions pictures taken on different samples. The picture is taken through the objective x60 and the scale is represented (25 μ).

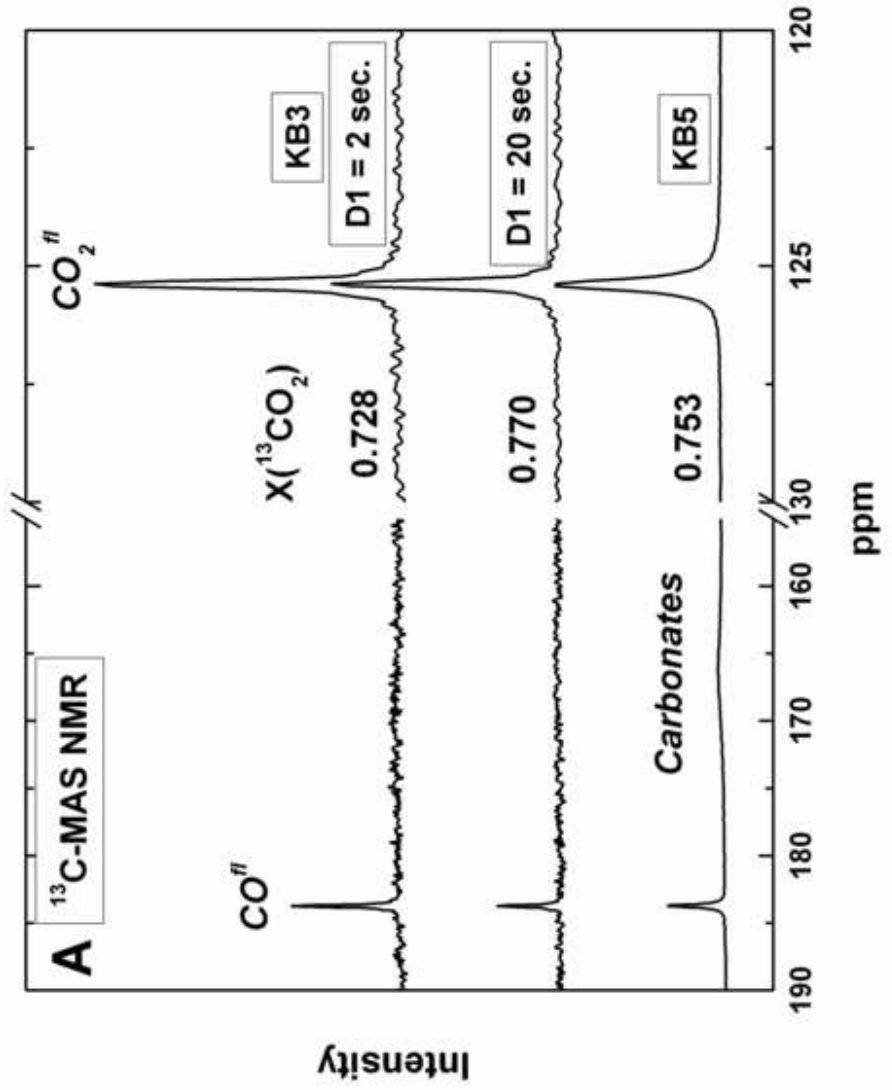

Figure 2A: ^{13}C-MAS NMR spectra for KB3 and 5. KB3 spectra were acquired with different recycle delay (D1 = 2 and 20 sec.). Several species are identified: 125, CO_2^{fl}; 180, CO^{fl}; 160-175 ppm, $CO_3^{2-\ melt}$. The $X(^{13}CO_2)$ for each is added and was calculated from the ratio of the integrated area for fluid species.

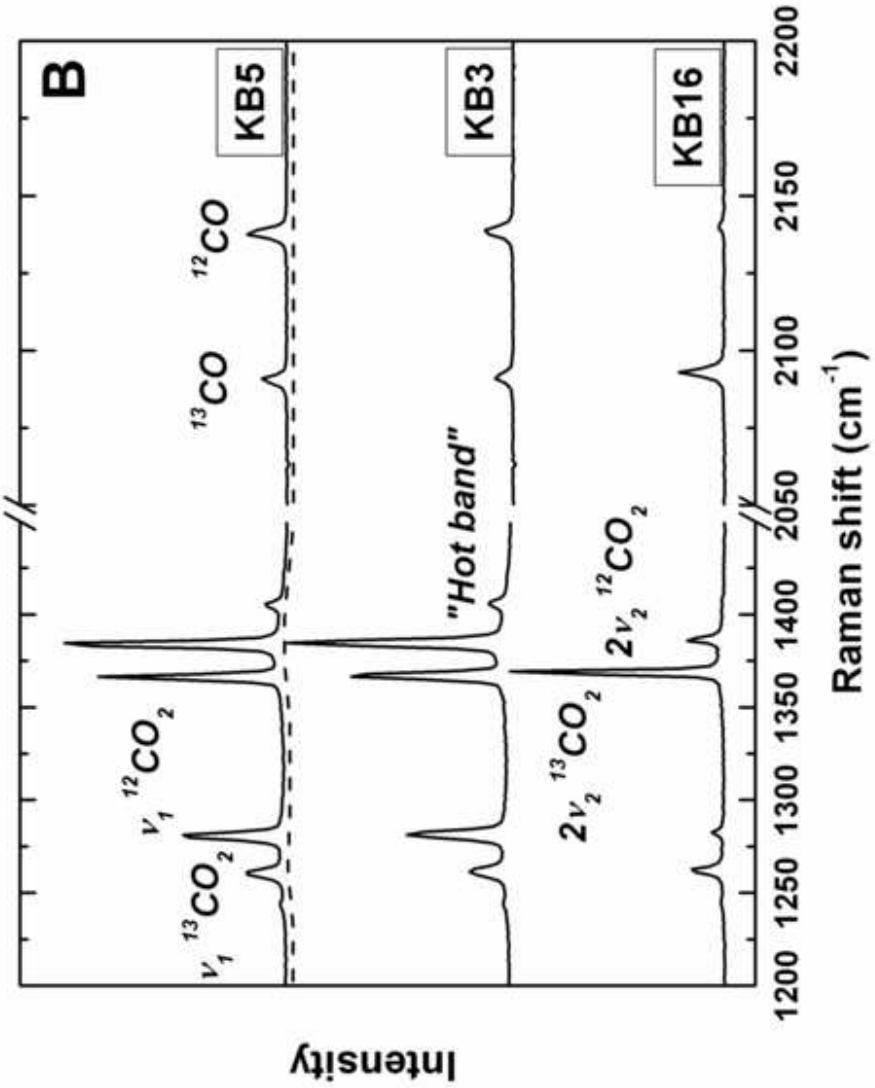

Figure 2B: Fluid inclusion Raman spectra showing the signature of the CO_2-CO gas mixture for ^{12}C and ^{13}C isotopes. The CO_2 Fermi is represented by 2 main vibrations: $2\nu_2$ (1385, 1360 cm^{-1} for $^{12}CO_2$ and $^{13}CO_2$) and ν_1 (1285, 1260 cm^{-1} for $^{12}CO_2$ and $^{13}CO_2$);

and accompanied by a “Hot band” vibration at 1405 cm^{-1}. CO shows 2 bands at 2140 and 2090 cm^{-1} for ^{12}C and ^{13}C respectively.

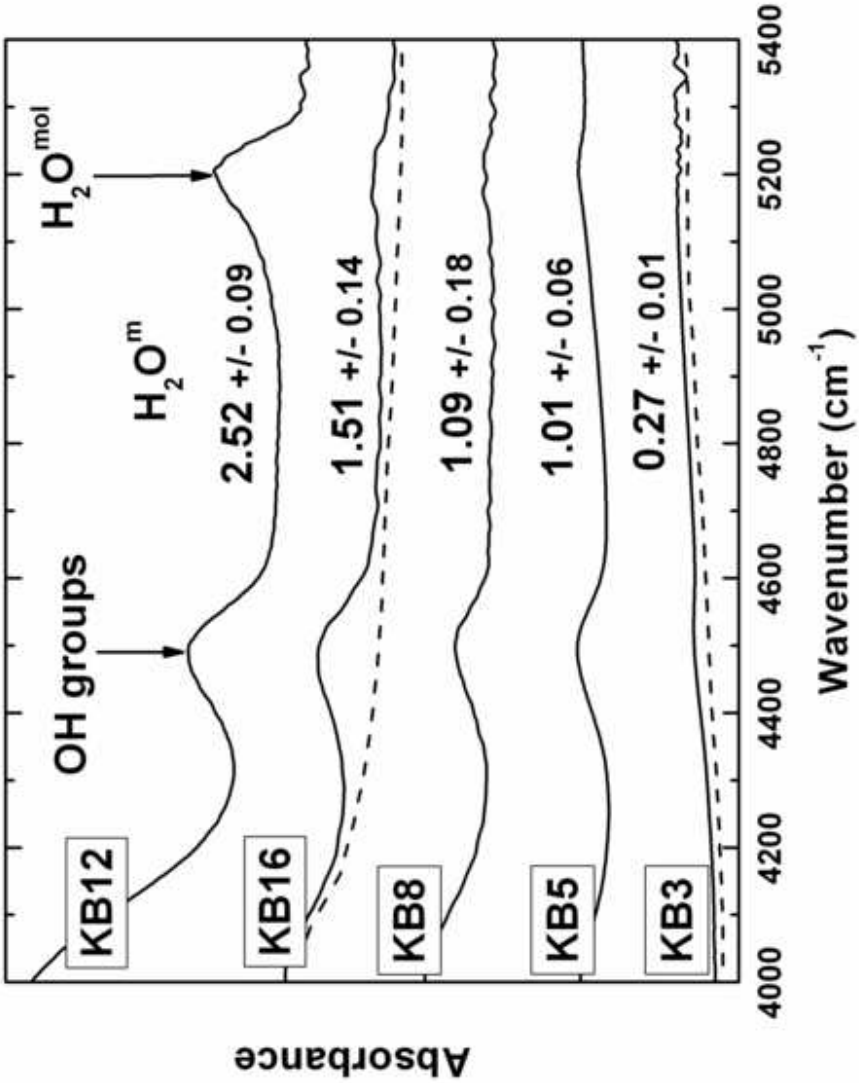

Figure 3: FTIR spectra showing the water vibrations: OH groups, 4500 cm^{-1}; H_2O^{mol}, 5200 cm^{-1}. The dashed line represents the baseline placed prior to integration of the vibration peaks. The water content (H_2O^m) is also indicated and was derived from Beer-Lambert approximation (see section 3.2.3 for detail).

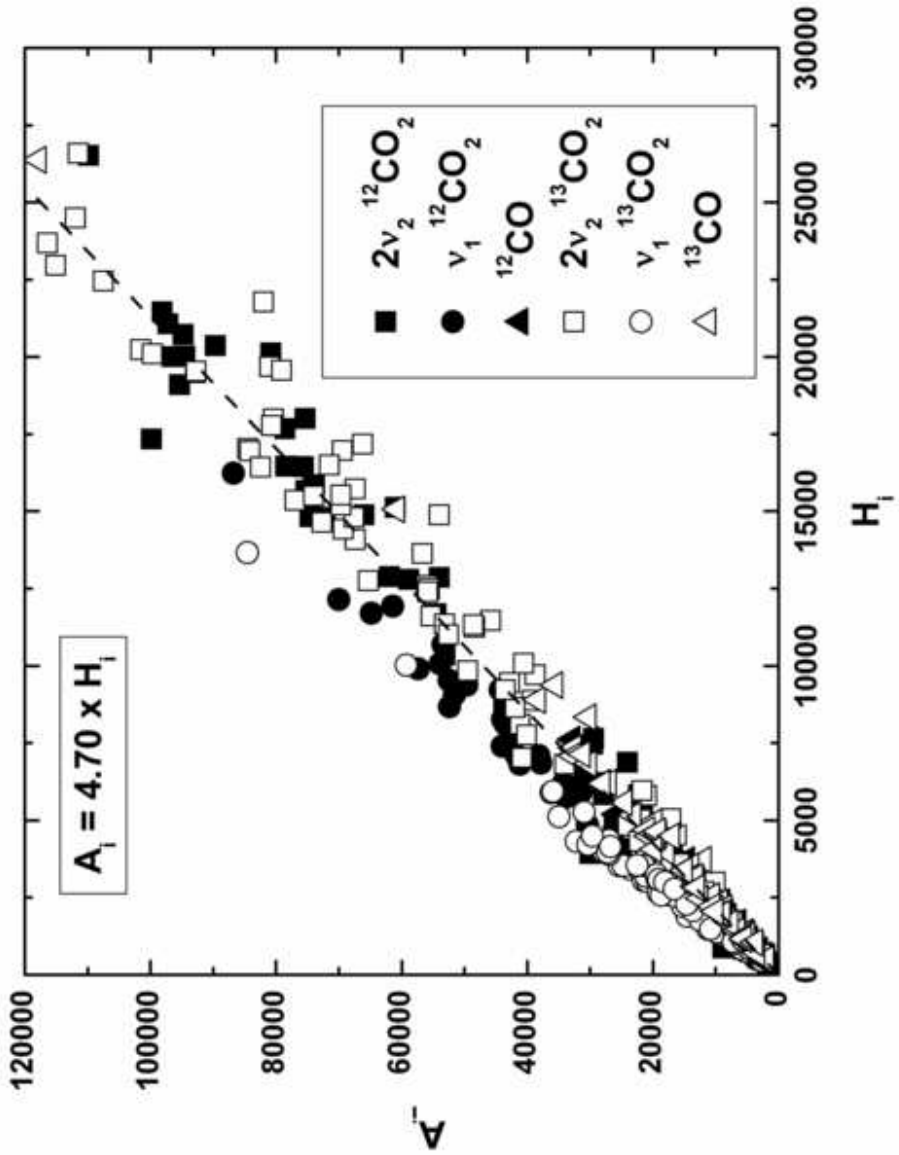

Figure 4: LRM peak area (A) versus peak height (H) for the observed gas resonances ($2\nu_2$ CO_2, square; ν_1 CO_2, circle; and CO, triangle) and for both isotopes (^{12}C, filled symbol; ^{13}C, open symbol).

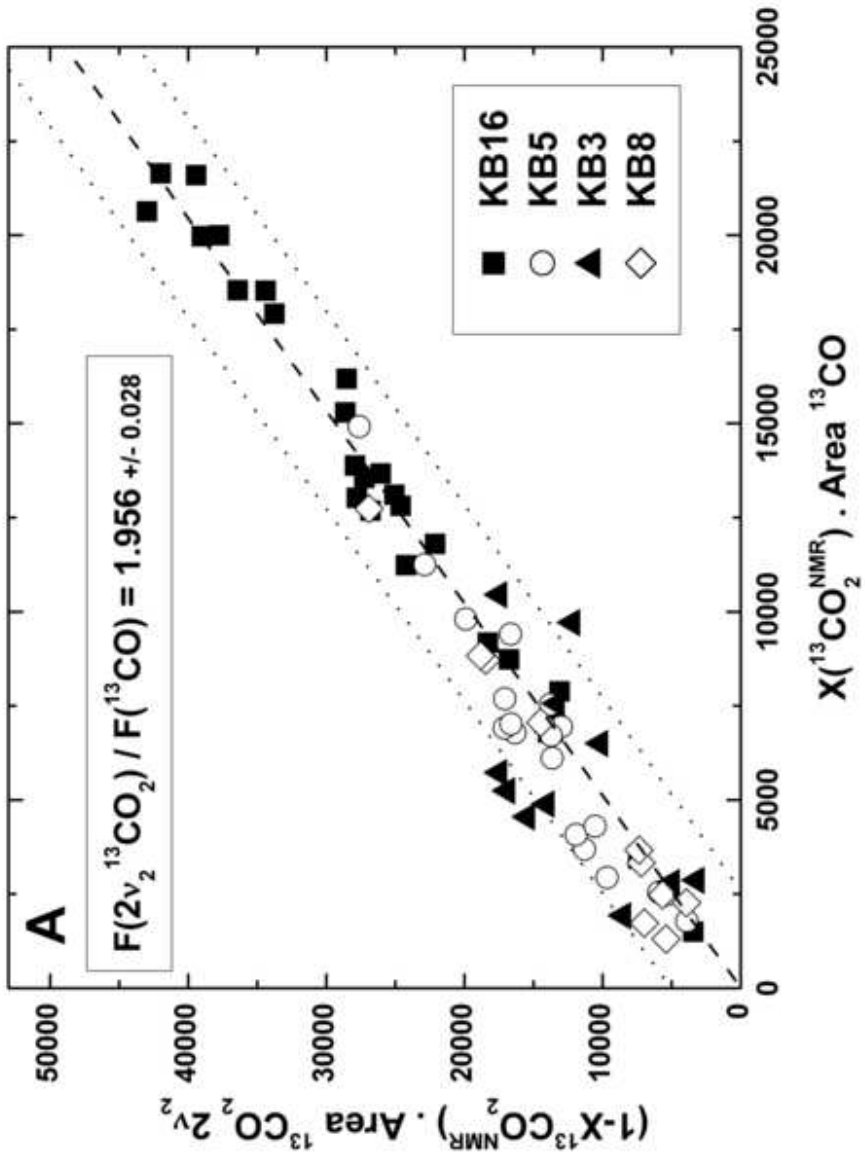
A
F(2ν2 13CO2) / F(13CO) = 1.956 +/- 0.028
KB16
KB5
KB3
KB8
(1-X13CO2NMR) . Area 13CO2 2ν2
X(13CO2NMR) . Area 13CO
0
5000
10000
15000
20000
25000
10000
20000
30000
40000
50000

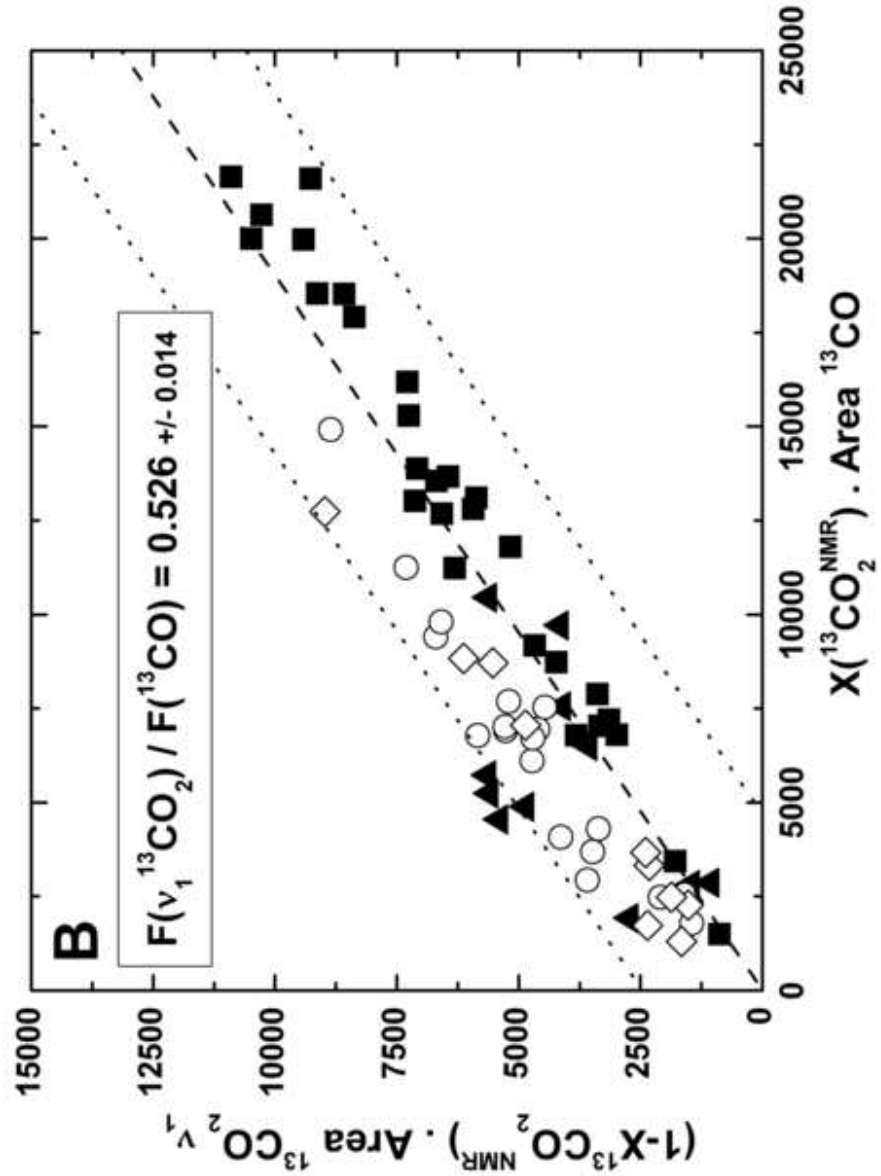
B
F(ν1 13CO2) / F(13CO) = 0.526 +/- 0.014
(1-X13CO2NMR) . Area 13CO2 ν1
X(13CO2NMR) . Area 13CO
0
2500
5000
7500
10000
12500
15000
0
5000
10000
15000
20000
25000

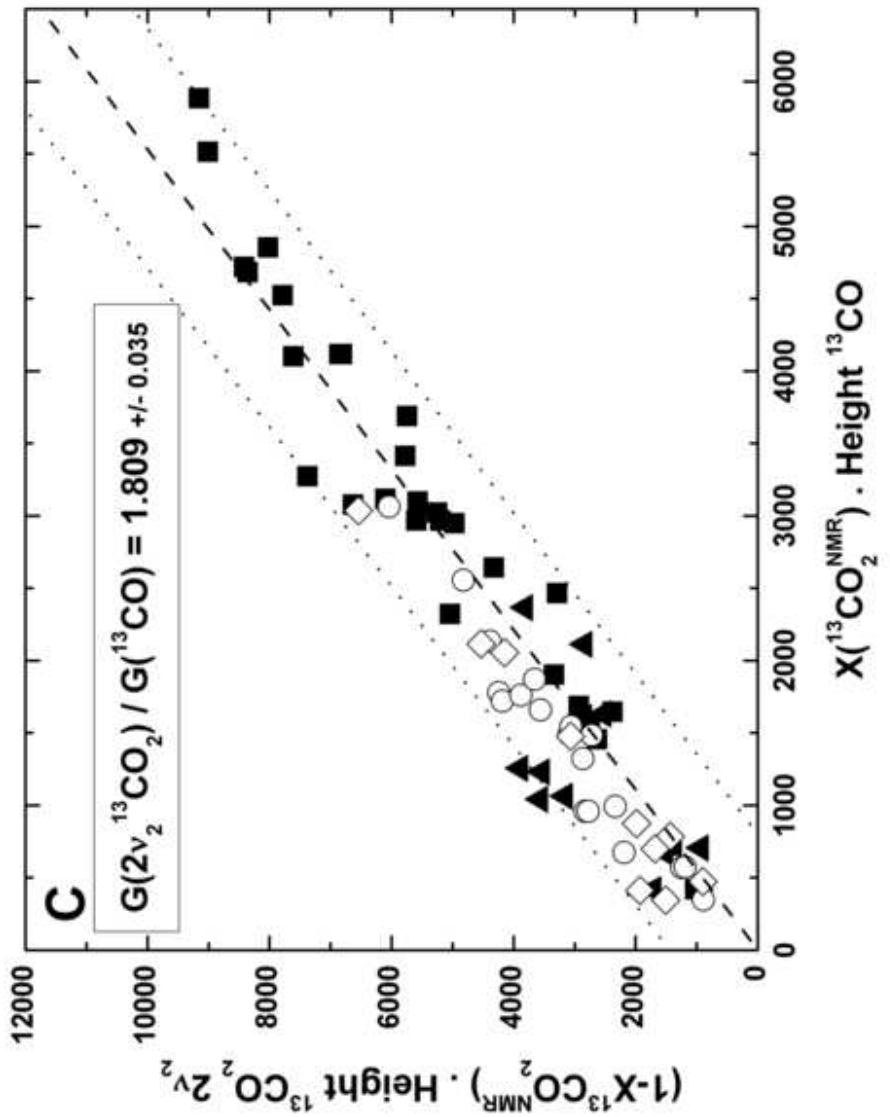
C
G(2ν2 13CO2) / G(13CO) = 1.809 +/- 0.035
(1-X13CO2NMR) . Height 13CO2 2ν2
X(13CO2NMR) . Height 13CO
0
2000
4000
6000
8000
10000
12000
1000
3000
5000

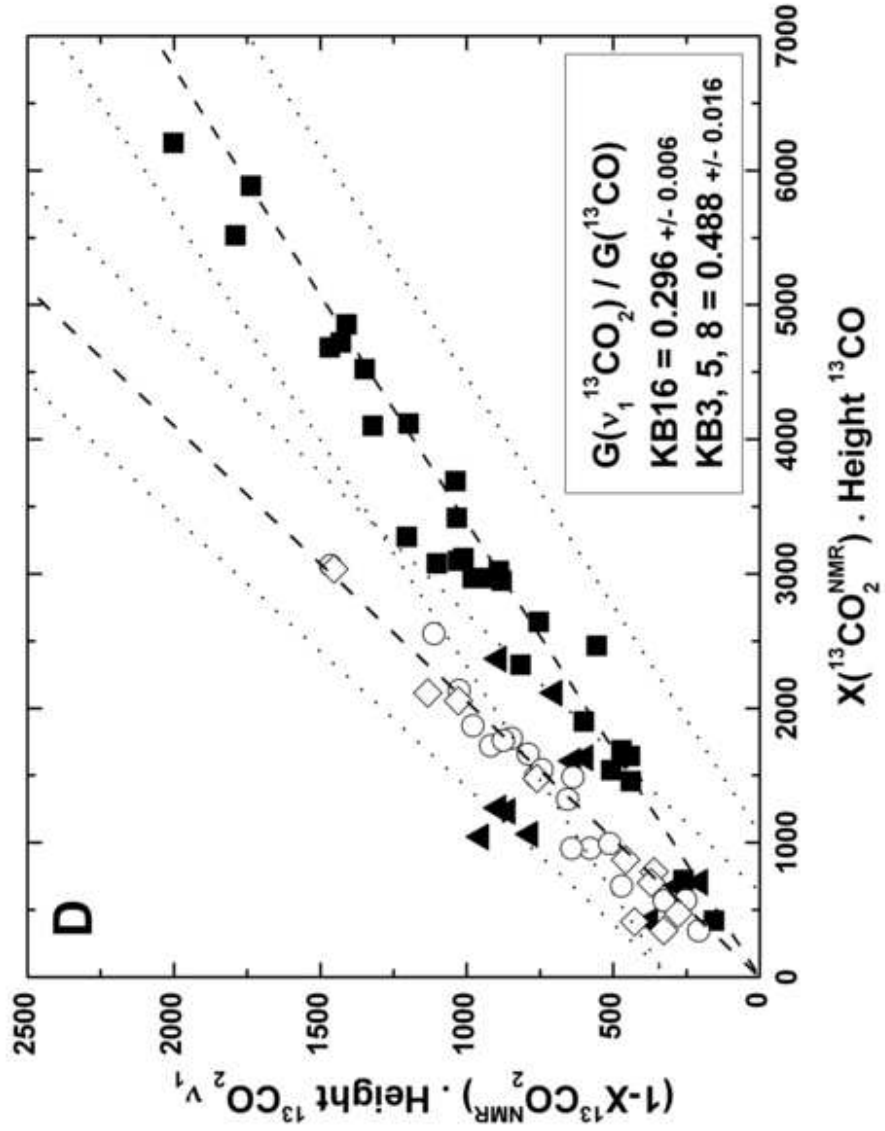

Figure 5: Raman quantification factor (F and G) calibration for ^{13}C isotopes. A, calibration for $F(2\nu_2\ CO_2)$ / F(CO); B, calibration for $F(\nu_1\ CO_2)$ / F(CO); C, calibration for $G(2\nu_2\ CO_2)$ / G(CO); D, calibration for $G(\nu_1\ CO_2)$ / G(CO).

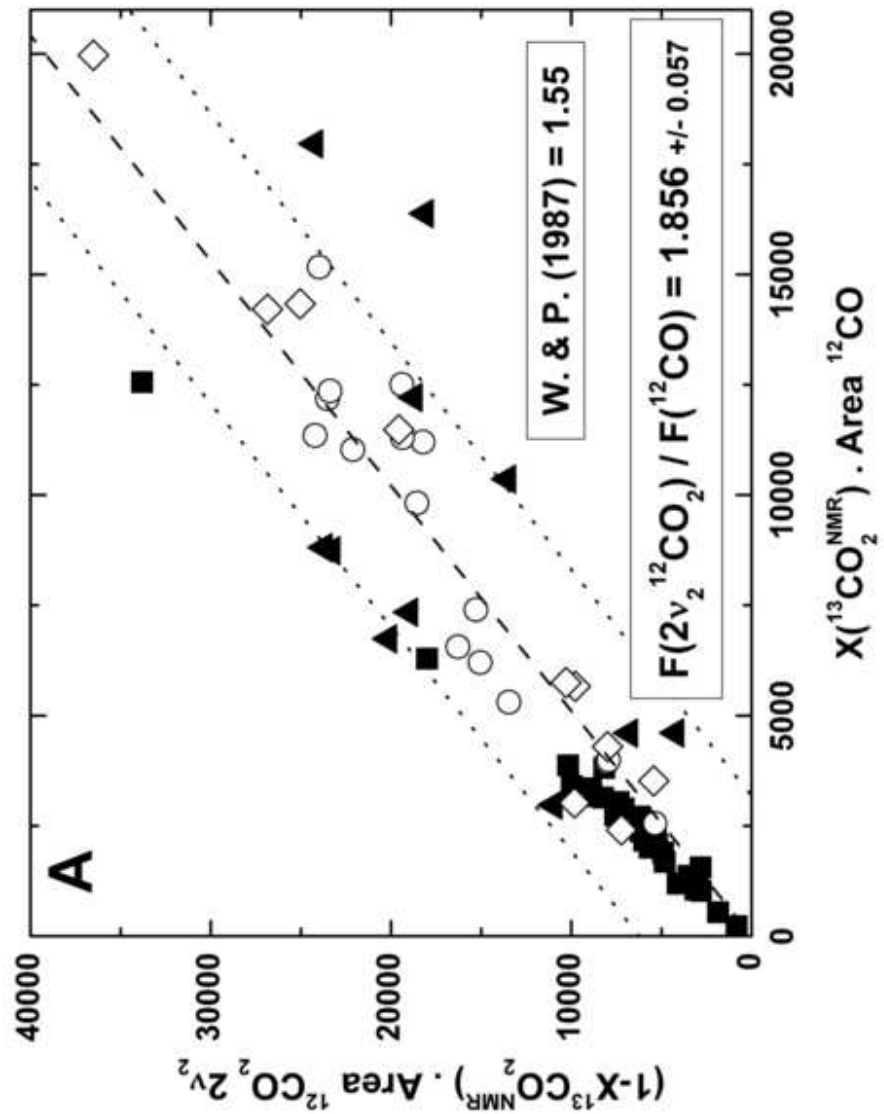
A
W. & P. (1987) = 1.55
F(2ν2 12CO2) / F(12CO) = 1.856 +/- 0.057
(1-X13CO2NMR) . Area 12CO2 2ν2
X(13CO2NMR) . Area 12CO
0
10000
20000
30000
40000
0
5000
10000
15000
20000

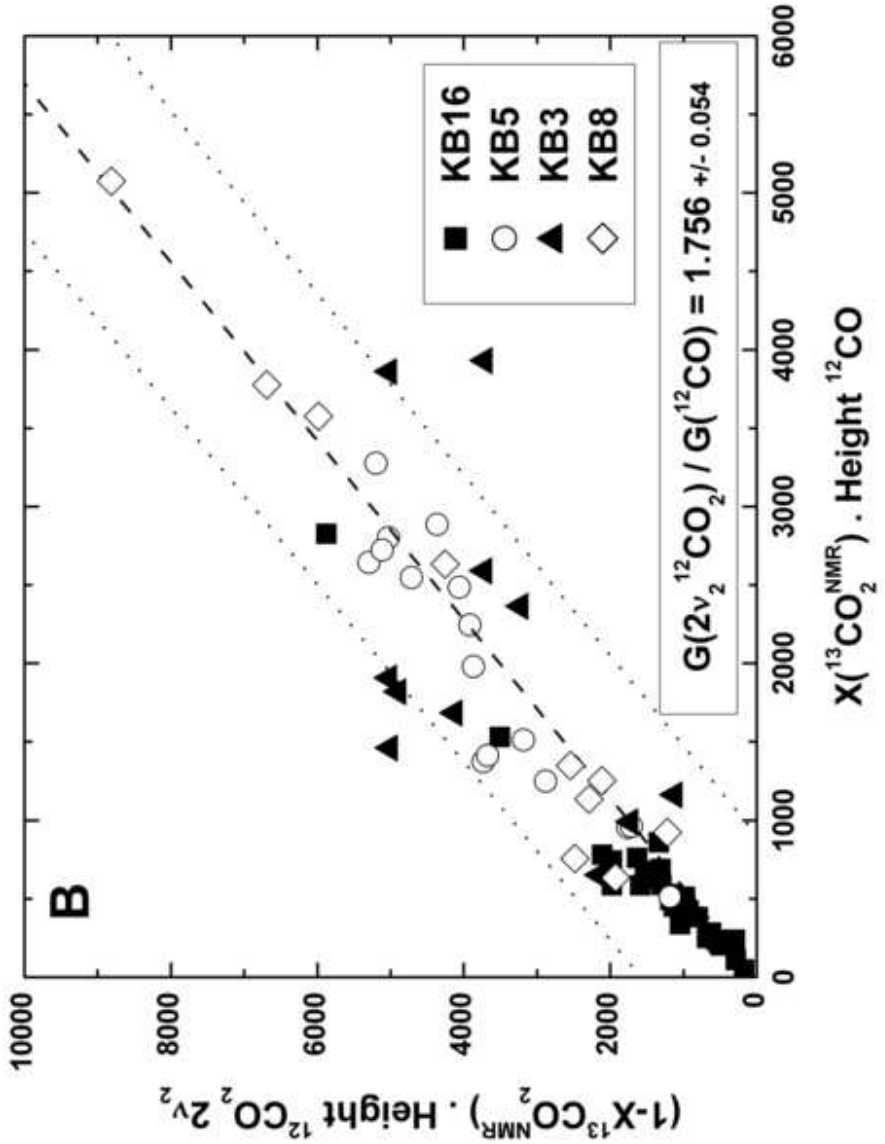

Figure 6: Raman quantification factor (F and G) calibration for ^{12}C isotopes. A, calibration for $F(2\nu_2\ CO_2)$ / F(CO); B, calibration for $G(2\nu_2\ CO_2)$ / G(CO). F factor value for $^{12}CO_2$ and ^{12}CO from Wopenka and Pasteris (1987) is also reported.

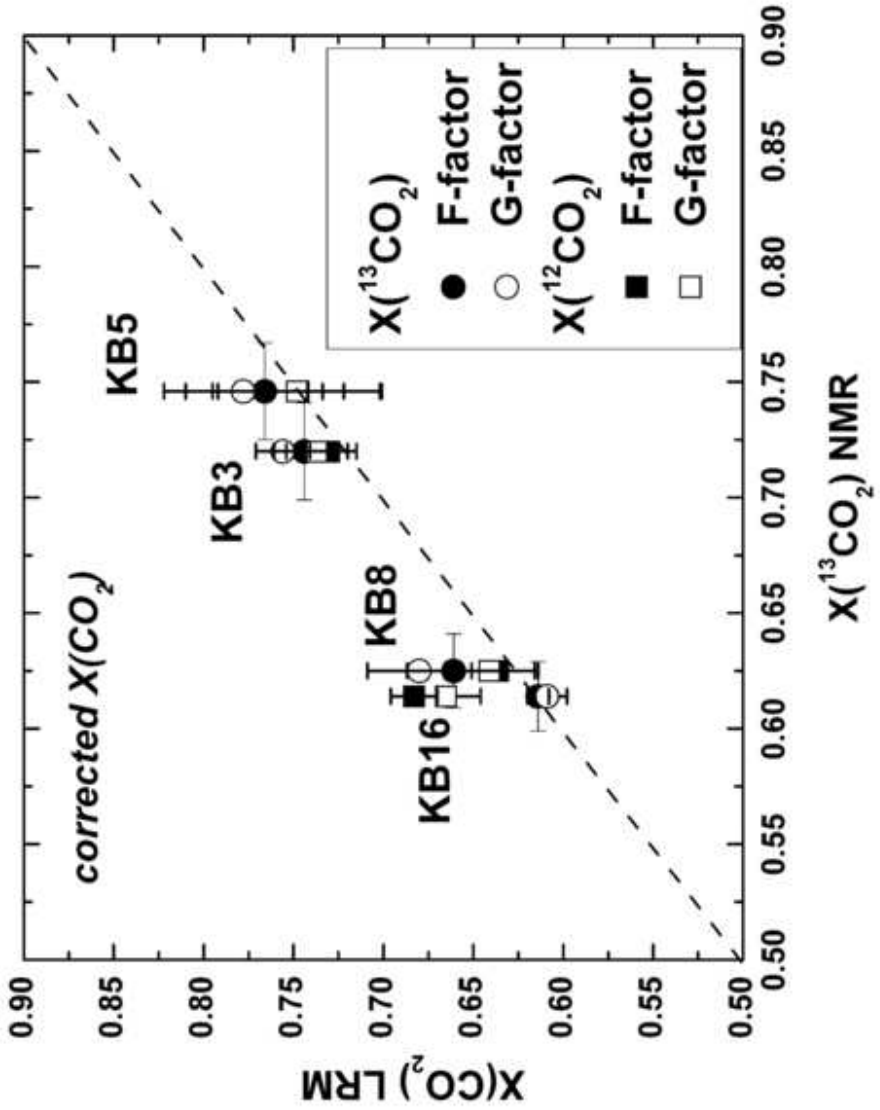

Figure 7: Recalculated $X(CO_2)$ from $2\nu_2$ CO_2 LRM calibration and plotted against $X(^{13}CO_2)$ measured from NMR. The circles and squares represent the $X(CO_2)$ for ^{13}C and ^{12}C respectively. Open symbols are obtained from G-factor and filled symbols from F-factor.

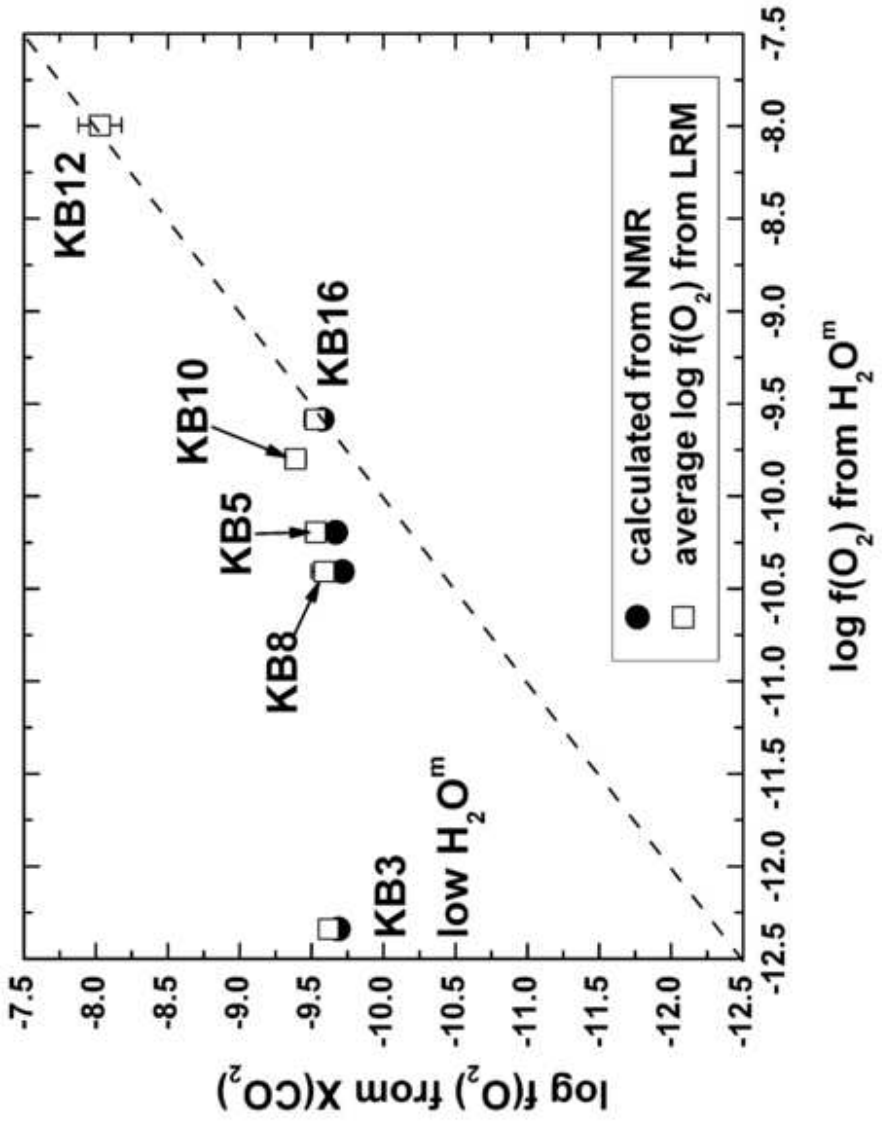

Figure 8: Log $f(O_2)$ calculated from X(CO_2) versus log $f(O_2)$ calculated from H_2O dissolved in the glass. The log $f(O_2)$ is calculated from X($^{13}CO_2$) NMR (circle) and the average values from LRM calibrations (square). NMR value is only available for KB16, 3, 5 and 8

Tables:

Sample	P^{tot} (MPa)	Temperature (°C)	$P(H_2)$ (bars)	H_2O^m	$X(^{13}CO_2)$ from NMR
KB3	210	1225	27	0.27 ±0.01	0.728[#] 0.770[#]
				Average	***0.749 ±0.029***
KB8	197	1250	56	1.09 ±0.18	0.668
KB5	210	1225	27	1.01 ±0.06	0.753
KB16	300	1250	40	1.51 ±0.14	0.689[#] 0.634[#]
				Average	***0.661 ±0.038***
KB10	320	1250	62	1.66 ±0.16	n.a.
KB12	313	1250	17	2.52 ±0.09	n.a.

Table 1: IHPV synthesis conditions for COH fluid bearing glasses. P^{tot} represents the final pressure during the experiment. The $P(H_2)$ is the partial pressure of H_2 at the experimental conditions. The H_2O^m was determined by FTIR analysis (see section 3.2.3 and Figure 2 for details). The error is calculated from standard deviation analysis. The $X(^{13}CO_2)$ was determined by peak integration of the ^{13}C-MAS NMR spectra. Value are uncorrected for the presence of H_2O in the fluid phase. [#] NMR spectra were acquired in different conditions. For KB3, two different values for D1 were used: 2 and 20 sec.. KB16 NMR spectra were acquired with 2 different pulse sequences: SPE and spin-echo (see section 2.3 for details).

Sample	$X(H_2O)$[a]	$X(^{13}CO_2)$ NMR	$X(^{13}CO_2)$ LRM				$X(^{12}CO_2)$ LRM			
			From F[d]		From G[d]		From F[d]		From G[d]	
		Corrected[b]	*Uncorrected*[c]	*Corrected*[b]	*Uncorrected*[c]	*Corrected*[b]	*Uncorrected*[c]	*Corrected*[b]	*Uncorrected*[c]	*Corrected*[b]
KB16	0.071 ±0.003	0.614 ±0.015	0.661 ±0.015	0.614 ±0.006	0.656 ±0.028	0.609 ±0.011	0.735 ±0.026	0.683 ±0.013	0.716 ±0.040	0.665 ±0.019
KB3	0.004 ±0.004	0.746±0.021	0.769 ±0.076	0.766 ±0.044	0.781 ±0.068	0.778 ±0.041	0.750 ±0.080	0.747 ±0.045	0.751 ±0.083	0.748 ±0.047
KB5	0.044 ±0.004	0.720 ±0.021	0.778 ±0.029	0.744 ±0.017	0.791 ±0.025	0.756 ±0.015	0.764 ±0.027	0.730 ±0.015	0.771 ±0.029	0.737 ±0.017
KB8	0.064 ±0.005	0.625 ±0.016	0.706 ±0.056	0.661 ±0.026	0.726 ±0.059	0.680 ±0.029	0.679 ±0.051	0.636 ±0.022	0.685 ±0.057	0.641 ±0.025
KB12	0.175 ±0.003	n.a.	0.932 ±0.025	0.769 ±0.018	0.910 ±0.027	0.751 ±0.019	0.911 ±0.014	0.752 ±0.010	0.903 ±0.004	0.745 ±0.004
KB10	0.078 ±0.003	n.a.	0.696 ±0.003	0.642 ±0.002	0.689 ±0.025	0.635 ±0.011	0.655 ±0.003	0.604 ±0.002	0.684 ±0.028	0.631 ±0.012

Table 2: Calculated species molar fractions in the fluid phase. [a] $X(H_2O)$ is derived from Dixon et al. (1995) relating total water content in the melt to fluid phase composition. [b] $X(CO_2)$ values are corrected for water content in the fluid phase (see section 4.3 for details). Error bars on the corrected values are based on error propagation from standard deviation. [c] Error on the uncorrected values is based the standard deviation from the fluid inclusion analyses by LRM. [d] $X(CO_2)$ is determined by LRM using both the calibration derived from peak integrated area (from F) and the calibration from peak height (from G). For clarity, X(CO) corrected values are not indicated but can be determined according to mass balance (Eq. (12)).

Sample	Log $f(O_2)$ from H_2O^m	Log $f(O_2)$ from $X(^{13}CO_2)$ NMR	Log $f(O_2)$ from $^{13}CO_2$ LRM		Log $f(O_2)$ from $^{12}CO_2$ LRM		Average log $f(O_2)$ from LRM
			From F	From G	From F	From G	
KB16	**-9.58**	**-9.58 ±0.02**	-9.58	-9.60	-9.43	-9.51	**-9.53 ±0.08**
KB3	**-12.34**	**-9.69**	-9.59	-9.53	-9.68	-9.68	**-9.62 ±0.07**
KB5	**-10.19**	**-9.67**	-9.55	-9.48	-9.62	-9.58	**-9.53 ±0.07**
KB8	**-10.41**	**-9.72**	-9.56	-9.48	-9.67	-9.65	**-9.59 ±0.09**
KB12	**-8.00**	**n.a.**	-7.82	-8.08	-8.07	-8.16	**-8.03 ±0.15**
KB10	**-9.80**	**n.a.**	-9.33	-9.36	-9.49	-9.38	**-9.39 ±0.07**

Table 3: Recalculated $X(CO_2)$ from LRM fluid inclusions analyses: for ^{13}C and ^{12}C and from F and G calibration. The log $f(O_2)$ is also represented and calculated using the MRK equation from Shi and Saxena (1992) from $X(CO_2)$ or the H_2O^m in the glass.

Appendix: Data for fluid inclusion analyses by LRM

Inc.	Acq. (sec.)	$^{12}CO_2$ ($2\nu_2$ / ν_1)		$^{13}CO_2$ ($2\nu_2$ / ν_1)		CO (^{12}C / ^{13}C)	
		height	area	height	area	height	area
KB16-1	45	2000 / 617	8304 / 3191	9711 / 1640	38701 / 9991	380 / 3729	2368 / 11928
KB16-2	30	494 / 173	2434 / 876	3011 / 461	10102 / 2609	77 / 636	348 / 2283
KB16-3	60	3211 / 895	16681 / 5553	18010 / 2987	80405 / 19734	767 / 4716	3036 / 20500
KB16-4	60	5840 / 1880	27824 / 9286	26603 / 5283	111450 / 30956	1126 / 8342	4910 / 30250
KB16-5	25	3393 / 1220	17569 / 6686	21786 / 3557	82007 / 21057	804 / 4954	3290 / 19697
KB16-6	50	2376 / 864	12078 / 3913	14895 / 2409	53986 / 13798	579 / 3515	1811 / 13888
KB16-7 15 mW	30	846 / 359	5609 / 1853	4075 / 750	22475 / 4736	193 / 1186	810 / 5502
KB16-7 30 mW	30	874 / 482	8848 / 2862	7036 / 1309	40830 / 9296	363 / 2491	1801 / 10895
KB16-7 50 mW	30	2579 / 827	14199 / 4899	12762 / 2228	65275 / 15263	585 / 3998	2550 / 17847
KB16-7 75 mW	30	5841 / 1242	22307 / 8681	20246 / 3541	101534 / 25335	886 / 6228	4153 / 28016
KB16-7 100 mW	20	4690 / 1264	20909 / 8245	20107 / 3541	99656 / 24723	889 / 6228	4383 / 27092
KB16-7 125 mW	20	3873 / 1358	24108 / 8353	23701 / 4164	116390 / 27378	1047 / 7343	5774 / 32666
KB16-7 150 mW	20	3938 / 1701	30040 / 10580	27034 / 5129	138028 / 34957	1301 / 8901	5866 / 38371
KB16-7 150b mW	10	2779 / 838	15445 / 5223	14666 / 2602	72677 / 17516	649 / 4460	3125 / 19383
KB16-7 175 mW	10	334 / 9830	18139 / 7083	17051 / 3051	84461 / 21409	683 / 5166	3601 / 23133
KB16-7 200 mW	10	3475 / 1010	18255 / 6120	16965 / 3064	84165 / 21513	745 / 5580	4104 / 24484
KB16-8 5 sec. 100 mW	5	839 / 293	5476 / 1907	4147 / 766	21892 / 5267	166 / 1094	833 / 5213

KB16-8 10 sec. 100 mW	10	1448 / 527	8267 / 3650	8115 / 1493	41130 / 11264	309 / 2330	1563 / 10273
KB16-8 20 sec. 100 mW	20	2879 / 1111	16165 / 7252	16452 / 3041	82428 / 20909	691 / 4686	3441 / 20993
KB16-8 30 sec. 100 mW	30	4499 / 1530	26266 / 9243	24687 / 4332	123978 / 32197	1023 / 7084	5079 / 32735
KB16-8 1 sec. 200 mW	1	325 / 115	2314 / 532	1564 / 290	8502 / 2219	69 / 432	540 / 2317
KB16-8 5 sec. 200 mW	5	1524 / 423	9183 / 2411	7774 / 1300	40089 / 8813	334 / 2205	1609 / 10295
KB16-8 10 sec. 200 mW	10	2753 / 920	16530 / 5211	15367 / 2760	76943 / 19046	644 / 4490	3217 / 20672
KB16-8 15 sec. 200 mW	15	4111 / 1313	24318 / 7817	22975 / 3983	115114 / 27790	957 / 6842	4757 / 30219
KB16-9		2893 / 887	15676 / 5982	15510 / 2628	73962 / 17320	775 / 4573	3488 / 19829
KB16-10		1617 / 496	9176 / 3032	8664 / 1391	41958 / 9842	363 / 2553	1909 / 10644
KB16-11		3843 / 1196	21742 / 7079	22470 / 3899	107504 / 26953	892 / 6202	4610 / 28046
KB16-12		1844 / 601	10303 / 3567	9852 / 1771	49457 / 12481	433 / 2879	2074 / 13219
KB16-13	15	3252 / 1102	16330 / 5535	19573 / 3252	79102 / 19426	723 / 4656	3094 / 19192
KB16-13ss	45	10357 / 3343	53109 / 16842	n.a. / 10038	n.a. / 59270	2316 / 15074	9520 / 60723
KB16-14	8	4813 / 1450	26139 / 9596	24841 / 4222	126875 / 30349	1154 / 7140	4812 / 31199
KB16-14ss	30	17351 / 4457	99806 / 30701	n.a. / 13680	n.a. / 84575	4278 / 26384	18999 / 117853
KB16-15	30	3080 / 932	14468 / 5223	16511 / 2890	71527 / 18637	510 / 4491	2873 / 16999
KB16-15ss	60	6238 / 2001	29406 / 9996	n.a. / 5910	n.a. / 36205	1184 / 9387	5156 / 35619
KB5-1	50	20381 / 9380	89675 / 49633	17197 / 3439	66211 / 23660	3721 / 2361	14644 / 9002
KB5-2	30	15138 / 6935	61013 / 33456	11477 / 2349	45827 / 14129	1823 / 1273	8240 / 4895

KB5-3	60	7140 / 3143	32488 / 16940	5044 / 1321	21944 / 8497	1268 / 758	5236 / 3300
KB5-4	120	11696 / 4861	54535 / 30385	8894 / 1910	39238 / 14574	1661 / 899	7051 / 3909
KB5-5	30	14895 / 6870	66007 / 37808	11255 / 2603	48371 / 16763	1877 / 1273	8711 / 5417
KB5-6	20	15680 / 7404	75261 / 43989	11622 / 2661	55338 / 19164	2630 / 1758	13037 / 8118
KB5-7	20	4808 / 2058	21714 / 11372	3618 / 847	15800 / 5869	680 / 461	3393 / 2369
KB5-8	10	12904 / 5757	61950 / 33836	9463 / 2077	42796 / 13649	200 / 13209	9827 / 5713
KB5-9	30	21474 / 10703	98124 / 53420	16984 / 3728	69393 / 21356	3512 / 2286	15071 9180
KB5-10	20	19114 / 8688	95341 / 52339	14431 / 3205	69287 / 21091	3382 / 2203	16178 / 10203
KB5-11	20	20737 / 10078	94789 / 53850	15738 / 3546	67404 / 21405	3614 / 2339	16409 / 9316
KB5-12	20	21085 / 9911	97213 / 57355	14819 / 3971	67574 / 27172	4350 / 2483	20143 / 12483
KB5-13	45	6935 / 3095	32177 / 16982	4833 / 1026	23994 / 6485	1276 / 762	5297 / 3388
KB5-14	30	15873 / 7112	73885 / 41747	11018 / 2586	52585 / 18692	2983 / 1974	14874 / 9226
KB5-14ss	55	n.a. / 12152	n.a. / 69995	19545 / 4511	92717 / 29648	5203 / 3391	25807 / 14933
KB5-15	40	16469 / 8118	78466 / 43480	12517 / 3098	55617 / 19079	3301 / 1981	15006 / 8908
KB5-15ss	60	n.a. / 11709	n.a. / 64825	17789 / 4161	80669 / 26725	4662 / 2831	21971 / 13013
KB5-16	15	17684 / 8276	78606 / 43887	12414 / 3012	55854 / 18095	3831 / 2052	16605 / 10001
KB5-16ss	30	n.a. / 16250	n.a. / 86769	24509 / 5940	111925 / 35932	7629 / 4065	32814 / 19802
KB3-1	30	20026 / 9082	94507 / 51580	14106 / 3432	67376 / 22288	2549 / 1647	11767 / 7001
KB3-2	10	8568 / 3840	43688 / 24315	6821 / 1493	34015 / 10834	871 / 558	3968 / 2581
KB3-3	10	16460 / 7709	75647 / 42242	12611 / 3123	56062 / 19355	2250 / 1422	9805 / 6526
KB3-4	25	20013 / 9536	96566 / 52409	15209 / 3550	69667 / 22384	5156 / 3160	23982 / 13963

KB3-5	25	14838 / 6828	74603 / 41171	11362 / 2544	53163 / 16360	3459 / 2146	16308 / 10099
KB3-6	20	12869 / 5934	53975 / 31415	10094 / 2372	40592 / 14206	3156 / 2179	13832 / 8676
KB3-7	20	19504 / 9080	92797 / 51610	15536 / 3558	69666 / 22485	2432 / 1678	11669 / 7643
KB3-8	40	14815 / 7097	72187 / 38120	11336 / 2792	48577 / 16549	5249 / 2822	21873 / 12967
KB8-1	60	7483 / 3548	29530 / 16999	5805 / 1285	20993 / 7106	1134 / 616	4524 / 2589
KB8-2	60	5805 / 2733	21706 / 11954	4530 / 985	16249 / 4992	953 / 517	3610 / 1954
KB8-3	50	3677 / 1787	16324 / 9127	2706 / 836	11880 / 4582	1383 / 709	5272 / 3391
KB8-4	50	12807 / 6213	58858 / 34200	9232 / 2288	43541 / 14633	3945 / 2212	17201 / 10576
KB8-5	60	18015 / 8172	75352 / 41880	12486 / 3099	55570 / 16644	5357 / 3078	21472 / 13047
KB8-6	60	7660 / 3662	29426 / 16429	5972 / 1376	21705 / 6996	2021 / 1308	8487 / 4984
KB8-7	40	6369 / 2871	30958 / 16632	4327 / 1085	22210 / 7205	1878 / 1176	8613 / 5490
KB8-8	60	20132 / 9239	80807 / 44283	13644 / 3411	56685 / 18455	5654 / 3168	21286 / 13232
KB8-9	60	6889 / 3129	24038 / 13350	5060 / 1113	17111 / 5624	1698 / 1050	6439 / 3724
KB8-10	60	26534 / 11939	109853 / 61420	19699 / 4377	81000 / 27012	7598 / 4545	29913 / 19077
KB12-2	20	17317 / 7867	96300 / 50440	9043 / 2083	48671 / 15382	1091 / 383	4424 / 1826
KB12-1	60	2110 / 921	9773 / 5399	966 / 253	5020 / 1995	125 / 67	578 / 127
KB10-1	60	903 / 417	3219 / 1737	617 / 130	2318 / 686	260 / 139	906 / 513
KB10-2	60	3221 / 1544	11647 / 6866	2117 / 450	7884 / 2934	774 / 566	3336 / 1779